

# Space Weather®

# <del>-</del>

#### RESEARCH ARTICLE

10.1029/2025SW004633

#### **Key Points:**

- Peak 2.0 MeV fluxes from coronal mass ejection-driven storms at L = 4.5 and 6.5 are 1.3 and 2.4 times larger than those from high speed solar wind streams
- Large flux events are associated with strong substorm activity, with AE > 300 nT from 14–26 hr before to 1.1– 2.5 days after zero epoch
- Large flux events are associated with low solar wind number density (n<sub>p</sub> < 4 cm<sup>-3</sup>) for several days following zero epoch

#### Correspondence to:

N. P. Meredith, nmer@bas.ac.uk

#### Citation:

Meredith, N. P., Bortnik, J., Hua, M., Cayton, T. E., Clilverd, M. A., Daggitt, T. A., & Bunting, K. A. (2025). Solar wind and geomagnetic conditions that lead to the largest relativistic electron fluxes in GPS orbit. *Space Weather*, 23, e2025SW004633. https://doi.org/10.1029/2025SW004633

Received 18 JUL 2025 Accepted 31 OCT 2025

#### **Author Contributions:**

Data curation: Nigel P. Meredith
Formal analysis: Nigel P. Meredith
Investigation: Nigel P. Meredith,
Jacob Bortnik, Man Hua, Thomas
E. Cayton, Mark A. Clilverd, Tom
A. Daggitt
Methodology: Nigel P. Meredith,
Jacob Bortnik, Man Hua, Thomas
E. Cayton, Mark A. Clilverd, Tom
A. Daggitt, Kaine A. Bunting

Concentualization: Nigel P Meredith

Project administration: Nigel
P. Meredith
Software: Nigel P. Meredith
Validation: Nigel P. Meredith, Kaine

A Runting

Visualization: Nigel P. Meredith Writing – original draft: Nigel P. Meredith, Jacob Bortnik, Man Hua,

© 2025. The Author(s).

This is an open access article under the terms of the Creative Commons

Attribution License, which permits use, distribution and reproduction in any medium, provided the original work is properly cited.

# Solar Wind and Geomagnetic Conditions That Lead to the Largest Relativistic Electron Fluxes in GPS Orbit

Nigel P. Meredith<sup>1</sup>, Jacob Bortnik<sup>2</sup>, Man Hua<sup>2</sup>, Thomas E. Cayton<sup>3</sup>, Mark A. Clilverd<sup>1</sup>, Tom A. Daggitt<sup>1</sup>, and Kaine A. Bunting<sup>1</sup>

<sup>1</sup>British Antarctic Survey, Natural Environment Research Council, Cambridge, England, <sup>2</sup>Department of Atmospheric and Oceanic Sciences, UCLA, Los Angeles, CA, USA, <sup>3</sup>Retired, Rio Rancho, NM, USA

**Abstract** Relativistic electrons are an important space weather hazard, being a major source of radiation damage to satellites and posing a risk to humans in space. We use approximately 20 years of data from the US Global Positioning System (GPS) satellite NS41 to determine the characteristics of the geomagnetic storms that lead to the largest relativistic electron fluxes in GPS orbit. The largest coronal mass ejection (CME)-driven events are associated with the solar wind having negative excursions of the IMF  $B_z$  with minimum values of  $\sim$ -14 nT two hours prior to zero epoch, defined as the time of the minimum in the *Dst* index, and strong *Dst* minima, reaching  $\sim$ -130 nT at zero epoch. In contrast, events driven by high speed solar wind streams (HSSs) are associated with smaller negative excursions of IMF  $B_z$  with minimum values of  $\sim$ -4 nT one to two hours prior to zero epoch and moderate *Dst* minima, reaching  $\sim$ -60 nT at zero epoch. Compared with HSS-driven events, peak E=2.0 MeV fluxes associated with CME-driven events are larger by factors of 1.3 at L=4.5 and 2.4 at L=6.5. Both the CME- and HSS-driven events are associated with enhancements in the solar wind number density and pressure prior to zero epoch. Following zero epoch the solar wind number density and pressure become low and substorm activity is enhanced for several days.

**Plain Language Summary** The Earth is surrounded by two donut shaped zones of very high energy electrons. The outermost of these zones is highly variable with the number of energetic particles changing by factors of 100 or more during enhanced space weather. Understanding the behavior of these so-called 'killer electrons' is important as they can damage satellites and pose a risk to humans in space. In this study we use approximately 20 years of data from the US Global Positioning System satellite NS41 to determine the conditions associated with the largest events. Our study reveals that there are many measurable features, both in space and on the ground, that occur before the peaks in the numbers of energetic electrons are observed. These findings may be used by satellite operators to help interpret the development of ongoing space weather events and to assess the likelihood of significant increases in the numbers of energetic electrons before they occur, enabling them to take appropriate precautionary measures if required.

#### 1. Introduction

Modern society is increasingly dependent on satellites and satellite technology for everyday activities such as communications, navigation, Earth observation, precision timing, and defense. For example, in 2024, the total revenue generated by the satellite industry was U.S. \$293 billion, an increase of 3% on the previous year (Satellite Industry Association, 2025). This ever growing infrastructure is increasingly vulnerable to the potentially damaging effects of space weather. The concern at government level in the UK is such that extreme space weather was added to the UK National Risk Register of Civil Emergencies in 2011 (Cabinet Office, 2012) where its likely impact was recently upgraded from moderate to severe (Cabinet Office, 2023).

Relativistic electrons (E > 0.5 MeV), often referred to as "killer electrons" (Graham, 1994), are a major source of radiation damage to satellites (Fennell et al., 2012; Gubby & Evans, 2002; Wrenn et al., 2002). They can penetrate spacecraft shielding and embed themselves in insulating materials and isolated metal components. Here, the charge can accumulate over time resulting in the build up of intense electric fields in and between materials to breakdown levels (Frederickson et al., 1991; Rodgers & Ryden, 2001). This can induce a current "spike" in electronic components leading to logic errors, erroneous data, phantom commands, loss of functionality and, in exceptional cases, serious harm to a satellite (e.g., Koons & Fennel, 2006).

MEREDITH ET AL. 1 of 28

Thomas E. Cayton, Mark A. Clilverd, Tom A. Daggitt, Kaine A. Bunting Relativistic electrons in near Earth space normally occupy two distinct zones known as the Earth's inner and outer radiation belts. The inner radiation belt, which typically occurs at geocentric distances of between 1.1 and 2.0 Earth radii ( $R_E$ ) in the Earth's magnetic equatorial plane, is relatively stable. Here significant variations only occur during the most intense geomagnetic storms (Baker et al., 2007). Further out, the outer radiation belt, which typically occurs at geocentric distances between 3 and 8  $R_E$ , is highly dynamic (e.g., Li & Hudson, 2019; Ripoll et al., 2020). In this region the fluxes of relativistic electrons may change by orders of magnitude on timescales ranging from minutes to weeks (e.g., Baker et al., 1994; Blake et al., 1992). This variability is controlled by a variety of transport, acceleration and loss mechanisms (e.g., Horne et al., 2005; Li & Hudson, 2019; Shprits, Elkington, et al., 2008; Shprits, Subbotin, et al., 2008; Thorne, 2010, Thorne et al., 2013), all of which become enhanced during geomagnetic storms, which are, themselves, ultimately driven by the Sun.

The response of the outer radiation belt to any individual geomagnetic storm is highly variable. For example, in a study of 276 moderate and intense geomagnetic storms Reeves et al. (2003) found that, while approximately half of the storms resulted in an increase in the flux of relativistic electrons, a quarter produced little or no change and a quarter resulted in a decrease. Recent statistical studies using Van Allen Probes observations also demonstrated that there is no strong dependence of the storm-time maximum electron fluxes on the storm intensity (Hua, Bortnik, & Ma, 2022; Zhang et al., 2021). Large relativistic electron flux enhancements following geomagnetic storms tend to be associated with high solar wind velocities and prolonged southward IMF Bz, sustained substorm activity, enhanced ULF and chorus wave power and enhanced fluxes of source and seed electrons (e.g., Blake et al., 1997; Hua & Bortnik, 2024; Iles et al., 2002; Jaynes et al., 2015; Li et al., 2015; Ma et al., 2024; Meredith et al., 2003; Miyoshi & Kataoka, 2008; O'Brien et al., 2001; Pinto et al., 2018). In contrast, periods of predominantly northward IMF  $B_z$  during the recovery phase do not result in significant relativistic electron flux enhancements (e.g., Iles et al., 2002; Jaynes et al., 2015; Li et al., 2015; Miyoshi & Kataoka, 2008; Pinto et al., 2018). Our current study focuses on the 50 largest events at L=4.5 and 6.5 in GPS orbit and thus does not include geomagnetic storms that are associated with little or no changes or reductions in the fluxes of relativistic electrons.

There are two principle solar drivers of geomagnetic storms: coronal mass ejections (CMEs) (e.g., Schwenn et al., 2005; Webb et al., 2000) and coronal holes (e.g., Krieger et al., 1973; Nolte et al., 1976). The largest geomagnetic storms are driven by interplanetary coronal mass ejections, the interplanetary counterpart of coronal mass ejections (e.g., Burlaga et al., 1982). These disturbances tend to track the solar cycle and have been found to peak at solar maximum (Webb & Howard, 1994) and up to 6 months to 1 year later (Robbrecht et al., 2009), depending on solar cycle. They typically have minimum *Dst* indices of less than -100 nT and are associated with recovery phases of the order of a couple of days.

Coronal holes are long-lasting dark areas on the Sun as observed in extreme ultraviolet and X-ray images (Cranmer, 2009). They are regions of open magnetic field and cooler plasma, leading to the production of high-speed solar wind streams (HSSs). HSSs are characterized by enhancements in the speed of the solar wind, with the speed typically exceeding 500 km s<sup>-1</sup> for 2–3 days and often maximizing above 800 km s<sup>-1</sup> (e.g., Denton & Borovsky, 2012). They may persist from one solar rotation to the next giving rise to a 27-day periodicity as viewed from the Earth. HSS-driven storms are most prevalent during the declining phase of the solar cycle (Burlaga & Lepping, 1977; Gonzalez et al., 1999) and usually result in weak to moderate geomagnetic storms (e.g., Tsurutani et al., 1995) with an average minimum *Dst* index of –40 nT (Richardson et al., 2006). However, they often have long recovery phases, typically lasting from 5 to 10 days, and, as a result, may deposit more energy, cumulatively, in the magnetosphere than larger CME-driven storms (Kozyra et al., 2006; Turner et al., 2006).

The enhancement of outer radiation belt fluxes during geomagnetic storms is driver dependent (Shen et al., 2017; Turner et al., 2019). At low L (L=3) relativistic electron acceleration events are driven solely by CME-driven storms, HSS-driven storms being ineffective in this region (Shen et al., 2017). Further out, at L=5, CME and HSS driven storms are, on average, roughly equally effective at relativistic energies (Shen et al., 2017). In a later study, covering a wider range of L shells, Turner et al. (2019) showed that, statistically, CME-driven storms are most effective at driving multi-MeV electron enhancements at lower L (L<5) while HSS-driven storms are most effective at higher L (L>5).

Global Navigation Satellite System (GNSS) satellites such as the US Global Positioning System, the European Galileo navigation system, the Russian GLONASS system, and the Chinese Beidou system operate in Medium

MEREDITH ET AL. 2 of 28

Earth Orbit (MEO) at altitudes between 19,000 and 24,000 km. They spend a large fraction of their orbit in the Earth's highly-variable outer radiation belt, typically crossing the magnetic equator near L = 4.2 and sampling higher L shells at higher latitudes.

GNSS enabled devices are used all over the world for a wide variety of applications, including navigation, positioning, tracking, mapping and timing. For example, in 2023 there were 5.6 billion GNSS devices in use and this is expected to rise to almost 9 billion by 2033 (EUSPA EO and GNSS Market Report, 2024). In 2023 the global downstream market revenue from both GNSS-enabled devices and services was 260 billion Euros and this is expected to grow to 580 billion Euros by 2033, largely fueled by expected revenues from added value services (EUSPA EO and GNSS Market Report, 2024). It is therefore important to have a comprehensive understanding of the environment encountered by satellites in GNSS-type orbits, including its extremes and the conditions leading to and associated with these extremes, to be able to better protect space assets operating in this region.

Meredith et al. (2023) determined the 1 in 10 and 1 in 100 year space weather events in GPS orbit as a function of location and electron energy. In a follow on study, they found that while the largest flux enhancements were caused by moderate to strong CME-driven geomagnetic storms, the majority of the events were caused by high speed solar wind streams, showing that both solar drivers are important for the most significant relativistic electron flux events (Meredith et al., 2024). In this paper we look at the specific characteristics of the CME- and HSS-driven storms that lead to the most significant electron flux enhancements in GPS orbit. We look at the solar wind and geophysical conditions and the characteristic responses of the MeV electrons at L=4.5 in the heart of the outer radiation belt and at L=6.5 on field lines that map to geosynchronous orbit. The paper is outlined as follows. In Section 2 we introduce the instrumentation and initial data analysis. In Section 3 we describe the results of the superposed epoch analysis before discussing the results and presenting the conclusions in Sections 4 and 5 respectively.

#### 2. Instrumentation and Data Analysis

The data used in this study were collected by the Burst Detector Dosimeter IIR (BDD-IIR) on board the US GPS satellite NS41. NS41 was launched on 10 November 2000 and operated in a circular orbit at an altitude of 20,200 km with an inclination of  $55^{\circ}$  and a period of 12 hr. It crossed the magnetic equator around L = 4.2 and sampled higher L shells at higher magnetic latitudes. For this study we use data from the entire mission, extending from 10 December 2000 to 25 July 2020.

BDD-IIR is a multi purpose silicon detector system (Cayton et al., 1998). It features eight individual channels of a "shield/filter/sensor" design that permits the detector to sample roughly half the celestial sphere while at the same time shielding the silicon sensor elements from most of the incident particle flux. Absorbers in front of the sensors determine the energy thresholds for measuring the incident particle fluxes. The aperture dimensions were chosen in an attempt to achieve equal counting rates in all channels. During on-orbit operation none of the BDD-IIR's channels appeared to saturate. Background counting rates were found to be well behaved.

For each week of data, mean values of the counting rates of the 8 channels were compiled from accumulations reported from L values larger than 20. Here L is the McIlwain L value calculated using the IGRF internal field and the Olson-Pfitzer quiet-time external field (Olson & Pfitzer, 1977). Except for weeks with one or more solar energetic particle (SEP) events, the weekly mean values were used for the background counting rates for each of the 2520 individual records. During SEPs, the background estimation followed the evolution of the SEP and were time dependent.

Any electron spectrum covering the energy range from 0.1 to 10 MeV can be folded with the response functions to predict counting rates in all eight channels due to that spectrum. Adding background counting rates to these yields a set of model counting rates that may be compared directly with the measured rates (corrected for the measured 6 ms dead-time). Best-fitting relativistic-Maxwellian spectra were determined by minimizing the sum of squared differences of a set of model counting rates (background plus ones due the spectrum of electrons) and the set of dead-time corrected measured counting rates. Each of the best-fitting spectra covers the energy range 0.1–10 MeV.

#### 2.1. Data Analysis

The NS41 BDD-IIR data used in this study were downloaded from the United States Department of Commerce's National Oceanic and Atmospheric Administration (NOAA) website. Each normal file includes 2,520 records each of duration 240 s, corresponding to one GPS-week of data. Each weekly file was examined, and excess

MEREDITH ET AL. 3 of 28

10.1029/2025SW004633



## **Space Weather**

records (almost always containing only "fill" values) were eliminated. Of the total of 1024 GPS-weeks during the lifetime of the mission, 31 were missing entirely, 3 included data for one day and 1 included data for two days. We used the data from the remaining 989 full weekly files in this study.

Electron differential fluxes at 10 energies (0.6, 0.8, 1.0, 1.6, 2.0, 3.0, 4.0, 5.0, 6.0, and 8.0 MeV) were written into separate files for each crossing of 12 equally-spaced L-shells between L=4.25 and L=7.00 (Meredith et al., 2023). NS41 crosses each of the specified L-shells as many as 8 times each day. The differential fluxes were then plotted as a function of time for each energy and L value to verify the absence of outliers and other anomalies in the data. Daily averaged fluxes were then compiled for each of the specified L-shells. For additional details regarding the data processing for BDD-IIR, see Meredith et al. (2023).

For our geomagnetic storm study, we first identified the 50 largest relativistic electron flux events throughout the entire mission at L=4.5 and L=6.5, as determined from the measured values of the E=2.0 MeV relativistic electron fluxes at L=4.5 and L=6.5 respectively. When compiling each list, we used the largest E=2.0 MeV electron flux associated with any given storm, thereby excluding the possibility of including the data from any given storm more than once. For each event we examined the behavior of the relativistic electron fluxes, the geomagnetic indices and the solar wind parameters over the preceding 10 days to identify the driver and strength of the associated geomagnetic storm as described in Meredith et al. (2024). CME-driven storms were confirmed using the Richardson and Cain list of near-Earth inter-planetary coronal mass ejections (Richardson & Cane, 2024) and high speed streams confirmed using the SIR/HSS event catalog presented in Grandin et al. (2019).

#### 3. Superposed Epoch Analysis

To compare and contrast the electron responses and solar wind and geophysical conditions during the top 50 CME- and HSS-driven events at L=4.5 and L=6.5 respectively, we conducted independent superposed epoch analyses for each event type and location. We used the individual measurements of the electron differential number fluxes, and hourly-averages of the solar wind parameters and geophysical indices from the NASA GSFC OMNI website (https://omniweb.gsfc.nasa.gov/). To investigate the potential cause of any observed relativistic electron dropouts as being due to magnetopause shadowing we also analyzed the position of the last closed drift shell (LCDS). This parameter was determined using the TS04 magnetic field model (Tsyganenko & Sitnov, 2005) and was calculated for equatorially mirroring particles, using a modification of the method given in Albert et al. (2018), explained in detail in Daggitt (2024).

We set the zero epoch at the Dst minimum of each storm. Although there are a number of different ways that a zero epoch could be defined, it is a clearly identifiable feature that lends itself to superposition. Prior to the Dst minimum the initial and main phases of the storm can last for a few hours to a few days (e.g., Mishra et al., 2024). We subsequently conducted the superposed epoch analysis as a function of the time relative to zero epoch going from -5 to +10 days in steps of 3 hr for the GPS data and steps of 1 hr for all the other parameters. Due to differences in the time intervals between individual L shell crossings we include all data points sampled within  $\pm 3$  hr of the center of each 3 hr time step in our analyses. This ensures that, on average, there are two L shell crossings for each individual event contributing to the superposed epoch analyses for each time stamp.

#### 3.1, L = 4.5

#### 3.1.1. CME-Driven Events

Twenty of the top fifty E = 2.0 MeV electron flux enhancements at L = 4.5 were associated with storms driven by coronal mass ejections (Meredith et al., 2024). We excluded the peak flux events of 6 October 2002, 24 July 2004, 11 November 2004, 20 January 2005, and 15 October 2012 since they were preceded or followed by an additional geomagnetic storm, with  $Dst_{min} \le -90$  nT in the five days either side of zero epoch, leaving us with 15 events for the analysis.

The results of the superposed epoch analysis for the CME-driven events at L=4.5 are presented in Figure 1. Key features of the solar wind parameters, geophysical indices and electron fluxes from the superposed epoch analysis are presented in the second and third columns of Table 1 and the start time, stop time and duration of intervals during which selected solar wind parameters and geophysical indices were predominantly above or below set levels are tabulated in the second, third and fourth columns of Table 2 respectively.

MEREDITH ET AL. 4 of 28

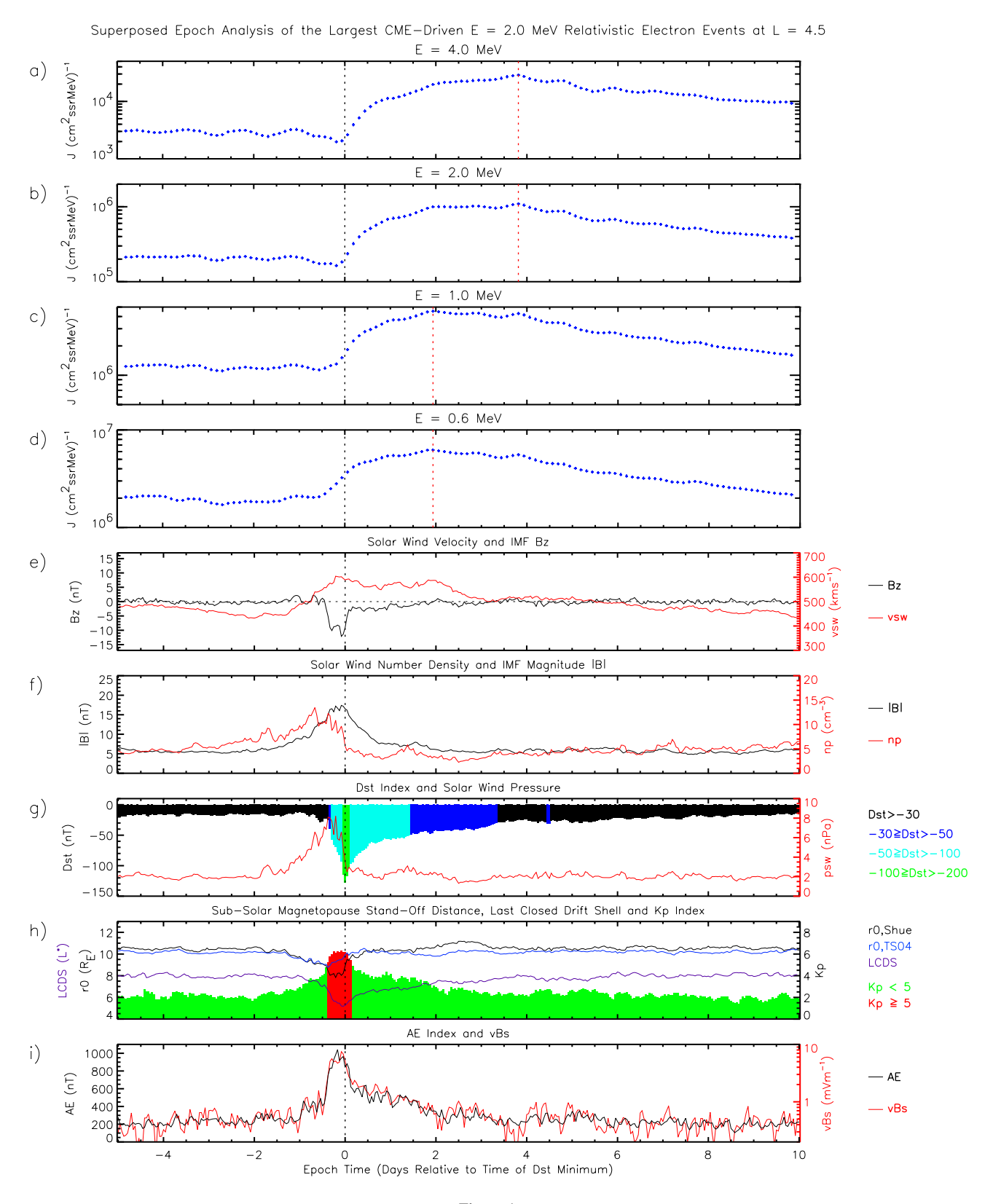


Figure 1.

MEREDITH ET AL. 5 of 28

10.1029/2025SW004633



### **Space Weather**

**Table 1** *Key Features of the Solar Wind Parameters, Geophysical Indices and Electron Fluxes From the Superposed Epoch Analyses for the CME- and HSS-Driven Events at L=4.5* 

	CME-driven events		HSS-driven events		
Parameter	$t_{epoch}$	Value	$t_{epoch}$	Value	
$n_{p,\max}$	-16 hr	13.5 cm <sup>-3</sup>	-13 hr	11 cm <sup>-3</sup>	
$r_{0,TS04,\min}$	−9 hr	$8.8~\mathrm{R}_E$	−7 hr	$9.0~\mathrm{R}_E$	
$p_{sw,\max}$	−5 hr	8.2 nPa	−6 hr	5.1 nPa	
$v_{sw,\max}$	−5 hr	$604 \text{ km s}^{-1}$	+18 hr	$670 \text{ km s}^{-1}$	
$AE_{max}$	-4 hr	1,041 nT	−2 hr	805 nT	
IMF $ B _{\text{max}}$	−2 hr	17 nT	-8 hr	11 nT	
IMF $B_{z,\min}$	−2 hr	−12 nT	−1 hr	−4.1 nT	
$Kp_{\text{max}}$	−2 hr	6.3	6.3 —2 hr		
$LCDS_{\min}$	−1 hr	$L^* = 5.2$	−1 hr	$L^* = 6.3$	
$Dst_{\min}$	0	−127 nT	0	-63 nT	
$J(0.6MeV)_{\text{max}}$	+1.9 days	$6.2 \times 10^6 \text{ (cm}^2 \text{ssrMeV})^{-1}$	+1.6 days	$5.2 \times 10^6 \text{ (cm}^2 \text{ssrMeV)}^{-1}$	
$J(1.0MeV)_{\text{max}}$	+1.9 days	$4.5 \times 10^6 \text{ (cm}^2 \text{ssrMeV})^{-1}$	+2.7 days	$3.8 \times 10^6 \text{ (cm}^2 \text{ssrMeV)}^{-1}$	
$J(2.0MeV)_{\text{max}}$	+3.8 days	$1.1 \times 10^6 \text{ (cm}^2 \text{ssrMeV})^{-1}$ +2.8 days		$8.8 \times 10^5 \text{ (cm}^2 \text{ssrMeV)}^{-1}$	
$J(4.0MeV)_{\rm max}$	+3.8 days	$2.9 \times 10^4 \text{ (cm}^2 \text{ssrMeV})^{-1}$ +2.9 days $1.9 \times 10^4 \text{ (cm}^2 \text{ssrMeV})^{-1}$		$1.9 \times 10^4 \text{ (cm}^2 \text{ssrMeV})^{-1}$	

The solar wind number density,  $n_p$  (Figure 1f, red trace), and pressure,  $p_{sw}$  (Figure 1g, red trace), and the magnitude of the interplanetary magnetic field, IMF |B| (Figure 1f, black trace), start increasing from values typical of the quiescent solar wind (Ebert et al., 2009; Schwenn, 2006) about 2 days prior to zero epoch. The number density increases up to a peak of 13.5 cm<sup>-3</sup> 16 hr prior to zero epoch. The rapid increase in number density, seen at this time, is generally associated with the arrival of the CME shock (Kwon et al., 2018). However, we note that the superposed epoch analysis brings out the general trends and that the arrival of specific CME features relative to zero epoch may vary from event to event and thus become somewhat smoothed in the superposed epoch analysis as a result. Following the number density peak, IMF |B| continues to increase, maximizing 2 hr prior to zero epoch. This peak is characteristic of the transition region between the sheath and the CME ejecta (Liu et al., 2010). Subsequently, IMF |B| gradually returns to quiescent values and the number density rapidly falls to very low values, conditions which are typically associated with CME ejecta (Liu et al., 2010).

The solar wind speed,  $v_{sw}$  (Figure 1e, red trace), also starts increasing 2 days prior to zero epoch maximizing at 604 km s<sup>-1</sup> 5 hr before zero epoch and falling to values around 500 km s<sup>-1</sup> 3 days following zero epoch. The north-south component of the interplanetary magnetic field in GSM coordinates, IMF  $B_z$  (Figure 1e, black trace), turns rapidly southward 11 hr prior to zero epoch reaching a minimum value of -12 nT 2 hr before zero epoch before rapidly increasing to -2 nT over the next few hours then remaining predominantly weakly southward for the next 3 days.

In response to the disturbed solar wind conditions, the sub-solar magnetopause stand-off distance, as determined from the TS04 model,  $r_{0,TS04}$  (Figure 1h, blue trace), starts moving inwards 2 days before zero epoch reaching a minimum distance of 8.8  $R_E$  9 hr before zero epoch before returning to pre-storm levels around zero epoch. The last closed drift shell, LCDS, as determined from the TS04 model (Figure 1h, purple trace), remains at its pre-

Figure 1. Superposed epoch analysis for the CME-driven events at L=4.5. From top to bottom the panels show (a–d) the BDD IIR electron flux measurements at E=4.0, 2.0, 1.0 and 0.6 MeV respectively; (e) the solar wind velocity (red trace) and the IMF  $B_z$  (black trace); (f) the solar wind number density (red trace) and the IMF |B| (black trace); g) the Dst index (color-coded) and solar wind pressure (red trace); (h) the Kp index (color-coded) and the Shue et al. (1998) and TS04 sub-solar magnetopause positions (black and blue traces respectively) and the TS04 last closed drift shell (purple trace); (i) the AE index (black trace) and the product of the solar wind velocity and the southward component of IMF  $B_z$  (red trace). The vertical black dashed lines in (a–i) denote zero epoch and the vertical red dashed lines in (a–d) mark the time of the peak electron flux at the selected energy.

MEREDITH ET AL. 6 of 28

**Table 2**Duration of Selected Solar Wind Parameters and Geophysical Indices With Respect to Set Levels at L = 4.5

		CME-driven events			HSS-driven events		
Parameter	$t_{begin}$	$t_{end}$	Duration	$t_{begin}$	$t_{end}$	Duration	
$n_p < 4 \text{ cm}^{-3}$	+9 hr	+3.3 days	2.9 days	+3 hr	+4.9 days	4.8 days	
$v_{sw} > 550 \text{ km s}^{-1}$	-11 hr	+2.3 days	2.8 days	-11 hr	+3.7 days	4.2 days	
Dst < -30  nT	-8 hr	+3.3 days	3.6 days	-8 hr	+1.8 days	2.1 days	
AE > 300  nT	-23 hr	+2.0 days	3.0 days	-1.1 days	+2.5 days	3.6 days	
Kp > 3	-22 hr	+1.9 days	2.8 days	-1.0 days	+2.5 days	3.5 days	

storm values until 1 day before zero epoch when it moves rapidly inwards to  $L^* = 5.2$  one hour before zero epoch and then gradually moves out to pre-storm values over the next 4 days.

The Dst index (Figure 1g, color-coded) starts decreasing 10 hr prior to zero epoch, reaches a minimum of -127 nT at zero epoch, prior to gradually returning to quiet time values over the next 4–6 days. The events are associated with enhanced geomagnetic and substorm activity as monitored by the Kp and AE indices respectively. The Kp index is greater than 3 (Figure 1h, color coded) from 22 hr before to 1.9 days following zero epoch while the AE index (Figure 1i, black trace) is greater than 300 nT from 23 hr before to 2.0 days following zero epoch. Remarkably, the logarithm of the product of vBs (Figure 1i, red trace), where v is the velocity of the solar wind and Bs is the southward component of IMF Bz, taken to be zero when northward, shows a very similar trend to that followed by the AE index.

The flux of E=0.6 MeV electrons (Figure 1d) start increasing from their pre-storm values of  $\sim 2.0 \times 10^6$  cm<sup>-2</sup> s<sup>-1</sup> sr<sup>-1</sup> MeV<sup>-1</sup> at  $t_{epoch}=-0.5$  days, reaching a peak value of  $6.2 \times 10^6$  cm<sup>-2</sup> s<sup>-1</sup> sr<sup>-1</sup> MeV<sup>-1</sup> 1.9 days after zero epoch. The flux of E=0.6 MeV electrons subsequently gradually decline back toward quiet time values, 10 days following zero epoch. At higher energies the fluxes start rising from later times, just before zero epoch, and peak 1.9, 3.8 and 3.8 days following zero epoch at E=1.0, 2.0, and 4.0 MeV (Figures 1a–1c respectively). The fluxes of E=2.0 MeV electrons peak at  $1.1 \times 10^6$  cm<sup>-2</sup> s<sup>-1</sup> sr<sup>-1</sup> MeV<sup>-1</sup>.

The statistical properties of the flux of E=2.0 MeV electrons, the solar wind parameters and geophysical indices in the superposed epoch analysis of the CME-driven events at L=4.5 are shown in Figure 2. Prominent features observed in Figure 1 using the mean values are clearly visible in the upper and lower quartiles and median values, including the peaks prior to zero epoch in the solar wind pressure (Figure 2b), number density (Figure 2c), and IMF |B| (Figure 2d) and minima at or around zero epoch in the Dst index (Figure 2g) and IMF  $B_z$  (Figure 2e) respectively. Enhancements in the Kp and AE indices in Figure 1 are also seen prior to and following zero epoch in the upper and lower quartiles and median values (Figures 2h and 2i respectively). There is a large spread in solar wind velocities from 2 days prior to zero epoch to 6 days following zero epoch (Figure 2f), showing that CME-driven events are associated with a wide range of solar wind velocities. There is also a wide spread in the fluxes of E=2.0 MeV electrons prior to zero epoch (Figure 2a), of the order of a factor of 10, caused by differences in the pre-storm flux levels. However, the post-storm maxima are much more tightly constrained indicating that the fractional increase in flux associated with any one of the top CME-driven events will be largely determined by the pre-storm flux level.

To provide further information on the characteristics of the solar wind and the geomagnetic responses, Figure 3 presents cumulative distributions of the solar wind parameters and geophysical indices determined from the CME-driven events used in the superposed epoch analysis at L=4.5 for selected epoch time intervals (color-coded). The separation between the larger values of the solar wind number density (Figure 3a), pressure (Figure 3b) and IMF |B| (Figure 3d) typically observed in the day before zero epoch and the lower values observed following zero epoch are clearly visible. Furthermore, the solar wind number densities following zero epoch (Figure 3a, colored traces) are, for any given percentile, less than the pre-storm values (Figure 3a, gray dotted trace) in the bulk of the observations in the 4 days following zero epoch. In contrast, following zero epoch, the distributions of the solar wind pressure closely resemble the pre-storm values (Figure 3b) and the distributions of IMF |B| return to pre-storm values 2–3 days following zero epoch (Figure 3d). IMF  $B_z$  (Figure 3e) is southward in 75 % of the observations the day following zero epoch and falling to approximately 50 % of the observations

MEREDITH ET AL. 7 of 28

15427393, 2025, 11, Downloaded from https://gupubs.online/blary.witey.com/doi/10.1092/025SW004633 by NICE, National Institute for Health and Care Excellence, Wiley Online Library on [21/11/205]. See the Terms and Conditions (https://online/blary.witey.com/terms-and-conditions) on Wiley Online Library for rules of use; O A article are governed by the applicable Decay.

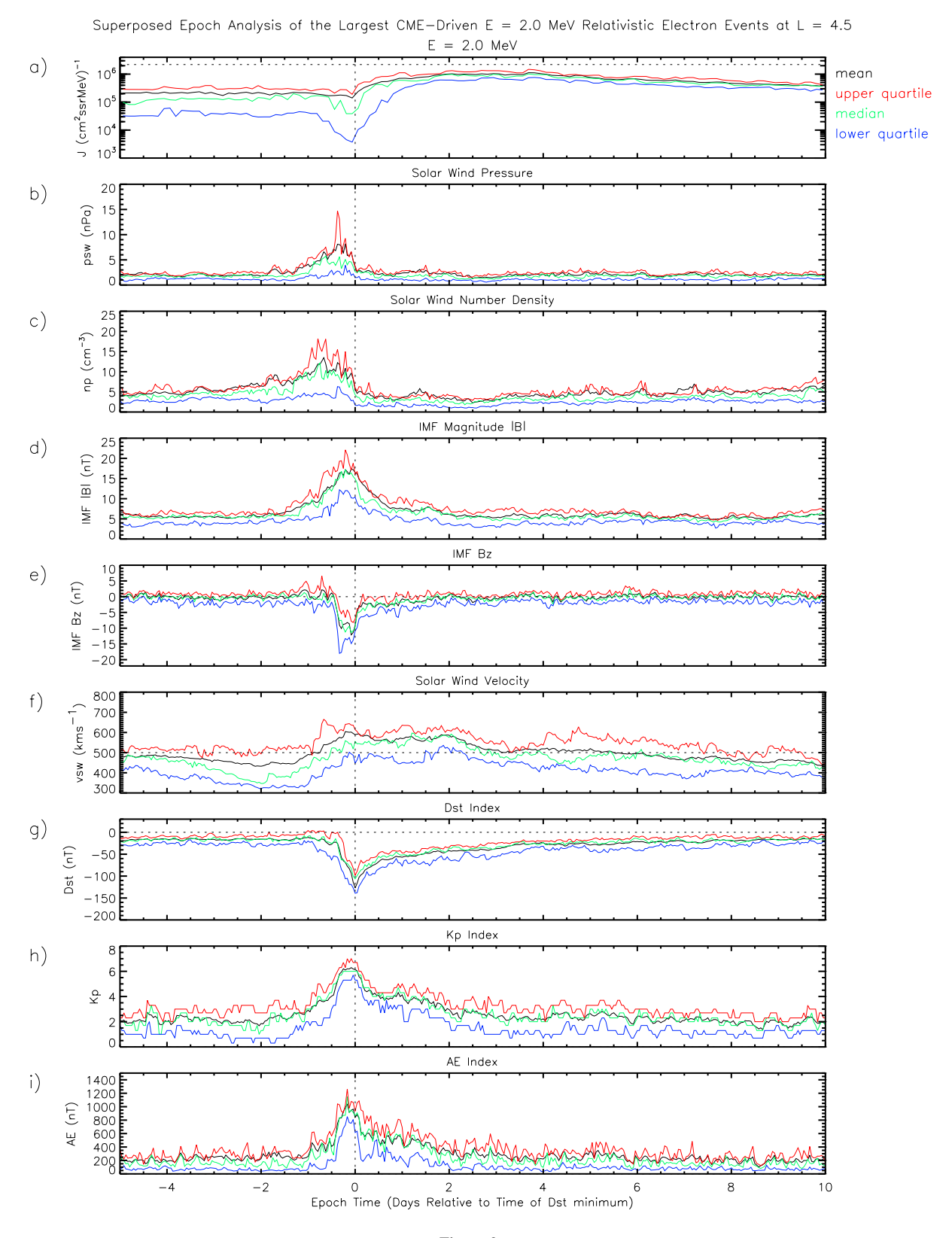


Figure 2.

MEREDITH ET AL. 8 of 28

from https://agupubs.onlinelibrary.wiley.com/doi/10.1029/2025SW004633 by NICE, National Institute for Health

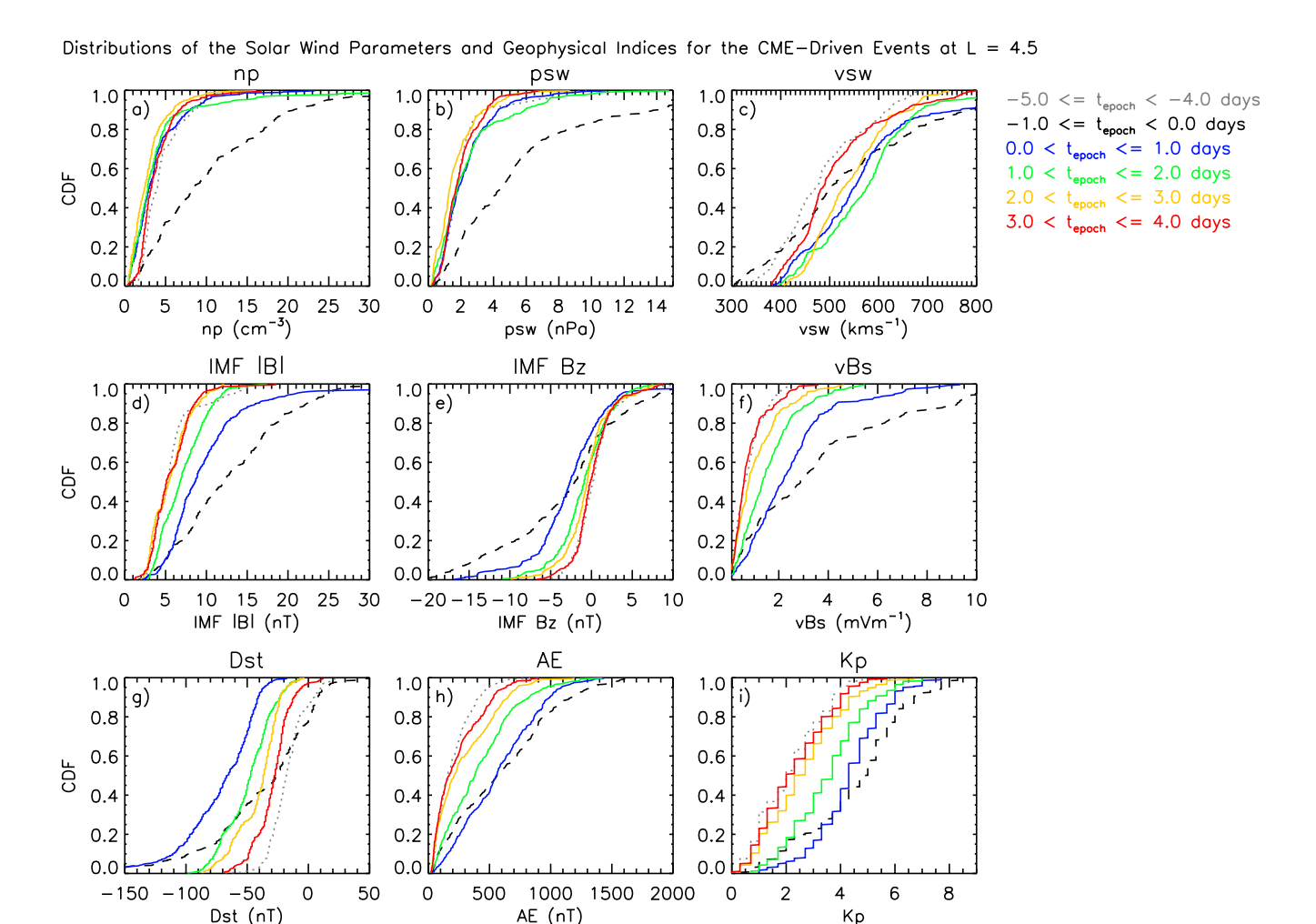


Figure 3. Cumulative distribution functions for the solar wind parameters and geophysical indices for the CME-driven events at L = 4.5 for selected epoch time windows (color-coded). From left to right and top to bottom the panels show (a) the solar wind density; (b) the solar wind pressure; (c) the solar wind velocity; (d) the IMF |B|; (e) the IMF  $B_r$ ; (f) the product of the solar wind velocity and the southward component of IMF  $B_r$ ; (g) the Dst index; (h) the AE index; and (i) the Kp index.

4 days following zero epoch. The distributions of AE (Figure 3h) and Kp (Figure 3i) are elevated and somewhat similar the day before and following zero epoch. They remain elevated, albeit with diminishing values, for any given percentile for the next 2–3 days.

#### 3.1.2. HSS-Driven Events

Thirty of the top fifty E = 2.0 MeV electron flux enhancements at L = 4.5 were associated with storms driven by high speed solar wind streams (Meredith et al., 2024). We excluded the peak flux event of 24 August 2003 since it was preceded by a strong geomagnetic storm 4 days prior to zero epoch. The results of the superposed epoch analysis for the selected twenty-nine HSS-driven events at L = 4.5 are presented in Figure 4, in the same format as Figure 1. The key features are presented in the fourth and fifth columns of Table 1 and the temporal extent of selected key features are presented in the fifth, sixth and seventh columns of Table 2.

Figure 2. Statistical properties of the flux of E = 2.0 MeV electrons, the solar wind parameters and geophysical indices in the superposed epoch analysis of the CME-driven events at L = 4.5. From top to bottom the panels show (a) the BDD IIR electron flux measurements at E = 2.0 MeV; (b) the solar wind pressure; (c) the solar wind number density; (d) the IMF |B|; (e) the IMF  $B_z$ ; (f) the solar wind velocity; (g) the Dst index; (h) the Kp index; and (i) the AE index. In each panel the arithmetic mean, the median and the upper and lower quartiles are coded black, green, red, and blue, respectively. The vertical black dashed lines in (a–i) denote zero epoch. The horizontal dashed line in (a) denotes the limiting flux of E = 2.0 MeV electrons determined from an independent extreme value analysis (Meredith et al., 2023).

MEREDITH ET AL. 9 of 28

15427390, 2025, 11, Downloaded from https://agupubs.onlinelibrary.wikey.com/doi/10.1092/025SW004633 by NICE, National Institute for Health and Care Excellence, Wiley Online Library on [21/11/2025]. See the Terms and Conditions (https://oilinelibrary.wikey.com/ems-and-conditions) on Wiley Online Library for rules of use; 0, Aarticle sar governed by the applicable the Cerems and Conditions (https://oilinelibrary.wikey.com/ems-and-conditions) on Wiley Online Library for rules of use; 0, Aarticle sar governed by the applicable the Cerems and Conditions (https://oilinelibrary.wikey.com/ems-and-conditions) on Wiley Online Library for rules of use; 0, Aarticle sar governed by the applicable the Cerems and Conditions (https://oilinelibrary.wikey.com/ems-and-conditions) on Wiley Online Library for rules of use; 0, Aarticle sar governed by the applicable the Cerems and Conditions (https://oilinelibrary.wikey.com/ems-and-conditions) on Wiley Online Library for rules of use; 0, Aarticle sar governed by the applicable the Cerems and Conditions (https://oilinelibrary.wikey.com/ems-and-conditions) on Wiley Online Library for rules of use; 0, Aarticle sar governed by the applicable the Cerems and Conditions (https://oilinelibrary.wikey.com/ems-and-conditions) on Wiley Online Library for rules of use; 0, Aarticle sar governed by the applicable the conditions (https://oilinelibrary.wikey.com/ems-and-conditions) on the conditions (https://oilinelibrary.wikey.com/ems-and-co

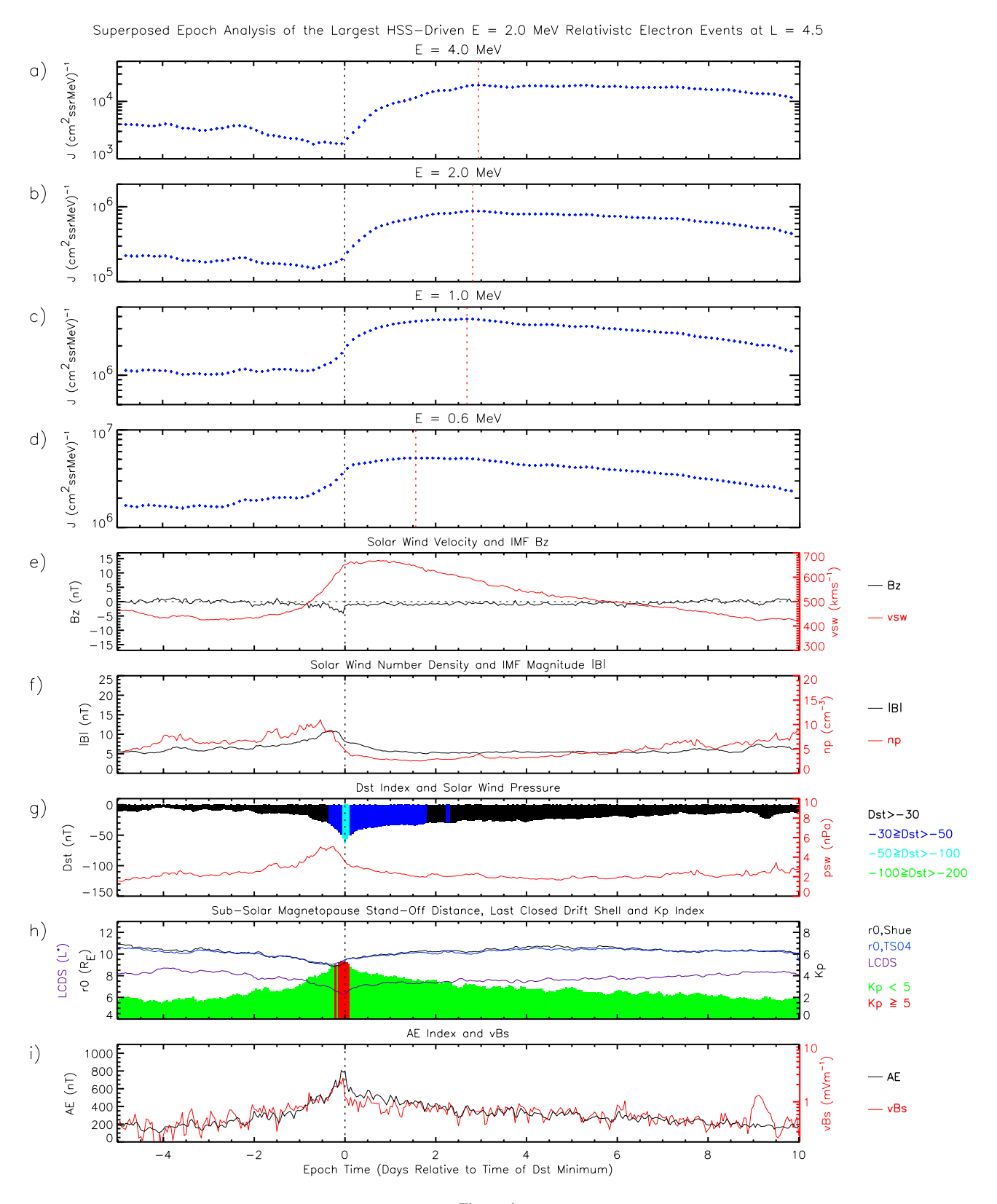


Figure 4.

MEREDITH ET AL. 10 of 28



## **Space Weather**

10.1029/2025SW004633

The solar wind number density (Figure 4f, red trace), pressure (Figure 4g, red trace) and IMF |B| (Figure 4f, black trace) start increasing from quiescent values about two days prior to zero epoch and subsequently maximize 6–13 hr prior to zero epoch. These features are consistent with the compression region which precedes the arrival of the high speed solar wind stream (Belcher & Leverett, 1971). The high speed stream itself is visible from  $\sim$ 6 hr prior to zero epoch to  $\sim$ 2 days following zero epoch. Fast and slow solar wind originate at different locations in the solar corona, with fast solar wind being associated with coronal holes and the slower solar wind with "quiet" areas of the Sun. The difference in origin has an impact on their solar wind properties (Feldman et al., 2005). For example, in the HSS itself a defined period of increased velocity (Figure 4e, red trace) is seen along with a lower number density (Figure 4f, red trace) and the B field is stable (Figure 4f, black trace). As the HSS outruns from the slower solar wind behind, a region of plasma rarefaction is formed (Siscoe et al., 1969). This region, which extends from 2 to 6 days post-zero epoch, is characterized by low density (Figure 4f, red trace), low IMF |B| (Figure 4f, black trace) and a decrease in velocity (Figure 4e, red trace) (Ďurovcová et al., 2024).

IMF  $B_z$  (Figure 4e, black trace) turns southward at  $t_{epoch} = -0.5$  days reaching a minimum of -4.1 nT 1 hr prior to zero epoch before rapidly increasing to -1.4 nT at zero epoch and then remaining predominantly very weakly southward for the next 7 days.

In response to the disturbed solar wind conditions, the sub-solar magnetopause stand-off distance (Figure 4h, blue trace) and last closed drift shell (Figure 4h, purple trace) start moving inwards  $\sim$ 3 days before zero epoch reaching minimum distances of 9.0 R<sub>E</sub> and  $L^*=6.3$ , 7 hr and 1 hr before zero epoch respectively. The magnetopause stand-off distance then starts to increase, returning to pre-storm levels approximately 2 days following zero epoch. The last closed drift shell, in contrast, takes longer to recover, returning to pre-storm levels about 8 days following zero epoch.

The *Dst* index (Figure 4g, color coded) starts decreasing about 2 days prior to zero epoch, reaches a minimum of -63 nT at zero epoch, prior to very gradually returning to pre-storm values over the next 8–9 days. The high speed stream events are associated with enhanced geomagnetic and substorm activity with *Kp* (Figure 4h, color-coded) greater than 3 from 1 day before to 2.5 days after zero epoch and *AE* (Figure 4i, black trace) greater than 300 nT from 1.1 days before to 2.5 days following zero epoch.

The flux of E=0.6 MeV electrons (Figure 4d) start increasing from their pre-storm values of  $\sim 2.0 \times 10^6$  cm<sup>-2</sup> s<sup>-1</sup> sr<sup>-1</sup> MeV<sup>-1</sup> at  $t_{epoch}=-2$  days, reaching a peak value of  $5.2 \times 10^6$  cm<sup>-2</sup> s<sup>-1</sup> sr<sup>-1</sup> MeV<sup>-1</sup> 1.6 days after zero epoch. The flux of 0.6 MeV electrons subsequently decline back toward pre-storm values, 10 days following zero epoch. At higher energies the fluxes start rising from later times around a day before zero epoch at E=1.0 MeV and shortly before zero epoch at E=4.0 MeV. The peak fluxes are also reached at later times, being seen 2.7, 2.8 and 2.9 days following zero epoch at E=1.0, 2.0, and 4.0 MeV (Figures 4a–4c respectively). The fluxes of E=2.0 MeV electrons peak at  $8.8 \times 10^5$  cm<sup>-2</sup> s<sup>-1</sup> sr<sup>-1</sup> MeV<sup>-1</sup> about 20% lower than during the CME-driven storms.

The statistical properties of the flux of E=2.0 MeV electrons, the solar wind parameters and geophysical indices in the superposed epoch analysis of the HSS-driven events at L=4.5 are shown in Figure 5 in the same format as Figure 2. Prominent features observed in Figure 4 using the mean values are again clearly visible in the upper and lower quartiles and median values, including the peaks prior to zero epoch in the solar wind pressure (Figure 5b), number density (Figure 5c) and IMF |B| (Figure 5d) and minima in the Dst index (Figure 5g) and IMF  $B_z$  (Figure 5e) at or around zero epoch. The solar wind speed (Figure 5f) is more tightly constrained than for the CME events with even the lower quartile exceeding 500 km s<sup>-1</sup> for over three days. Enhancements in the Kp and AE indices in Figure 5 are also seen prior to and following zero epoch in the upper and lower quartiles and median values (Figures 5h and 5i respectively). There is again a wide spread in the fluxes of E=2.0 MeV electrons prior to zero epoch (Figure 5a), which become much more tightly constrained following zero epoch.

Figure 4. Superposed epoch analysis for the HSS-driven events at L=4.5. From top to bottom the panels show (a–d) the BDD IIR electron flux measurements at E=4.0, 2.0, 1.0 and 0.6 MeV respectively; (e) the solar wind velocity (red trace) and the IMF  $B_z$  (black trace); (f) the solar wind number density (red trace) and the IMF |B| (black trace); (g) the Dst index (color-coded) and solar wind pressure (red trace); (h) the Kp index (color-coded) and the Shue et al. (1998) and TS04 sub-solar magnetopause positions (black and blue traces respectively) and the TS04 last closed drift shell (purple trace); (i) the AE index (black trace) and the product of the solar wind velocity and the southward component of IMF  $B_z$  (red trace). The vertical black dashed lines in (a–i) denote zero epoch and the vertical red dashed lines in (a–d) mark the time of the peak electron flux at the selected energy.

MEREDITH ET AL. 11 of 28

15427393, 2025, 11, Downloaded from https://gappubs.onlinebtrary.wiley.com/do/10.10929025SW004633 by NICE, National Institute for Health and Care Excellence, Wiley Online Library or [21/11/2025]. See the Terms and Conditions (https://onlinebtrary.wiley.com/ems-and-conditions) on Wiley Online Library for rules of use; OA articles are governed by the applicable (Crean Security of Care Excellence, Wiley Online Library of Care Excellence, Wiley On

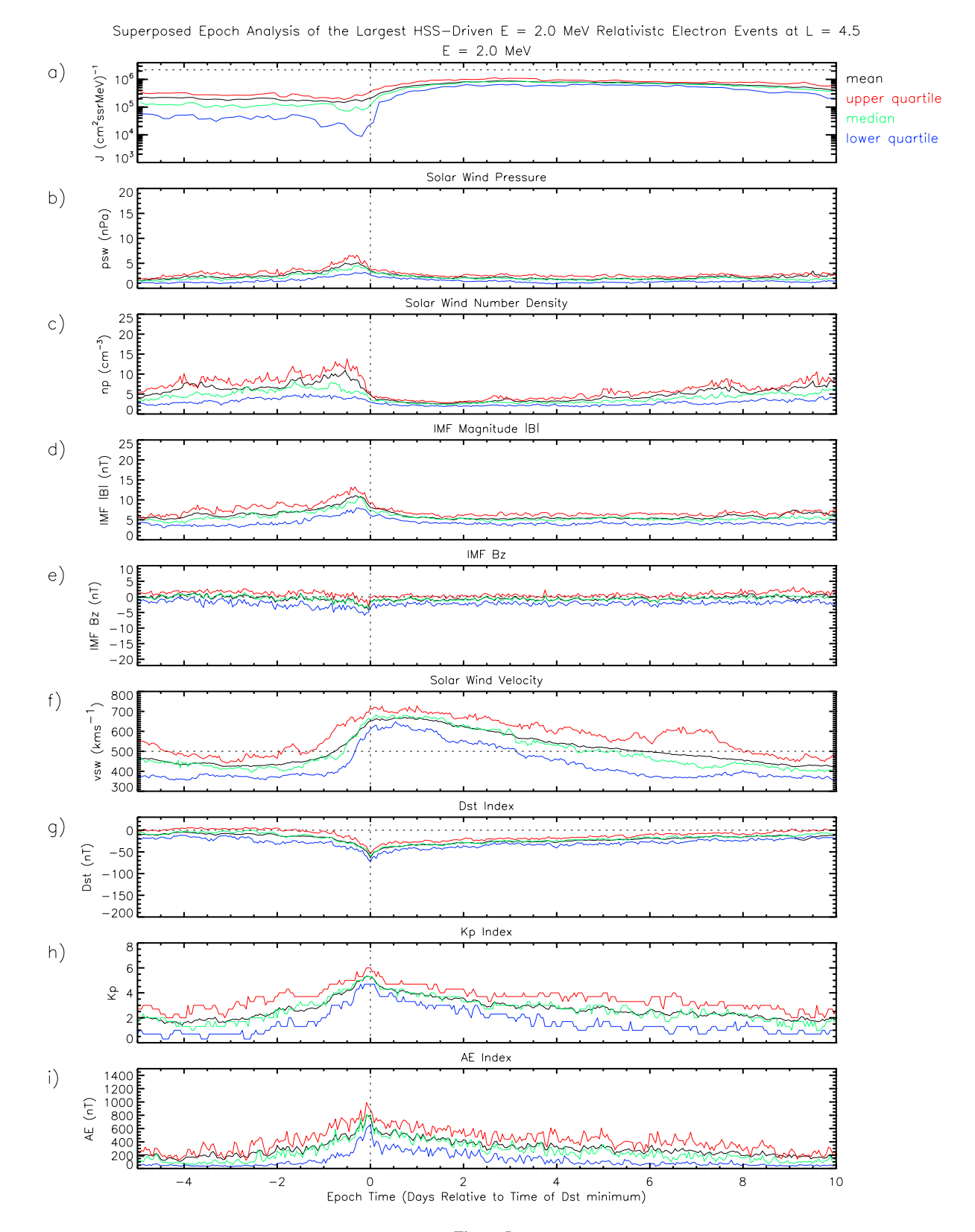
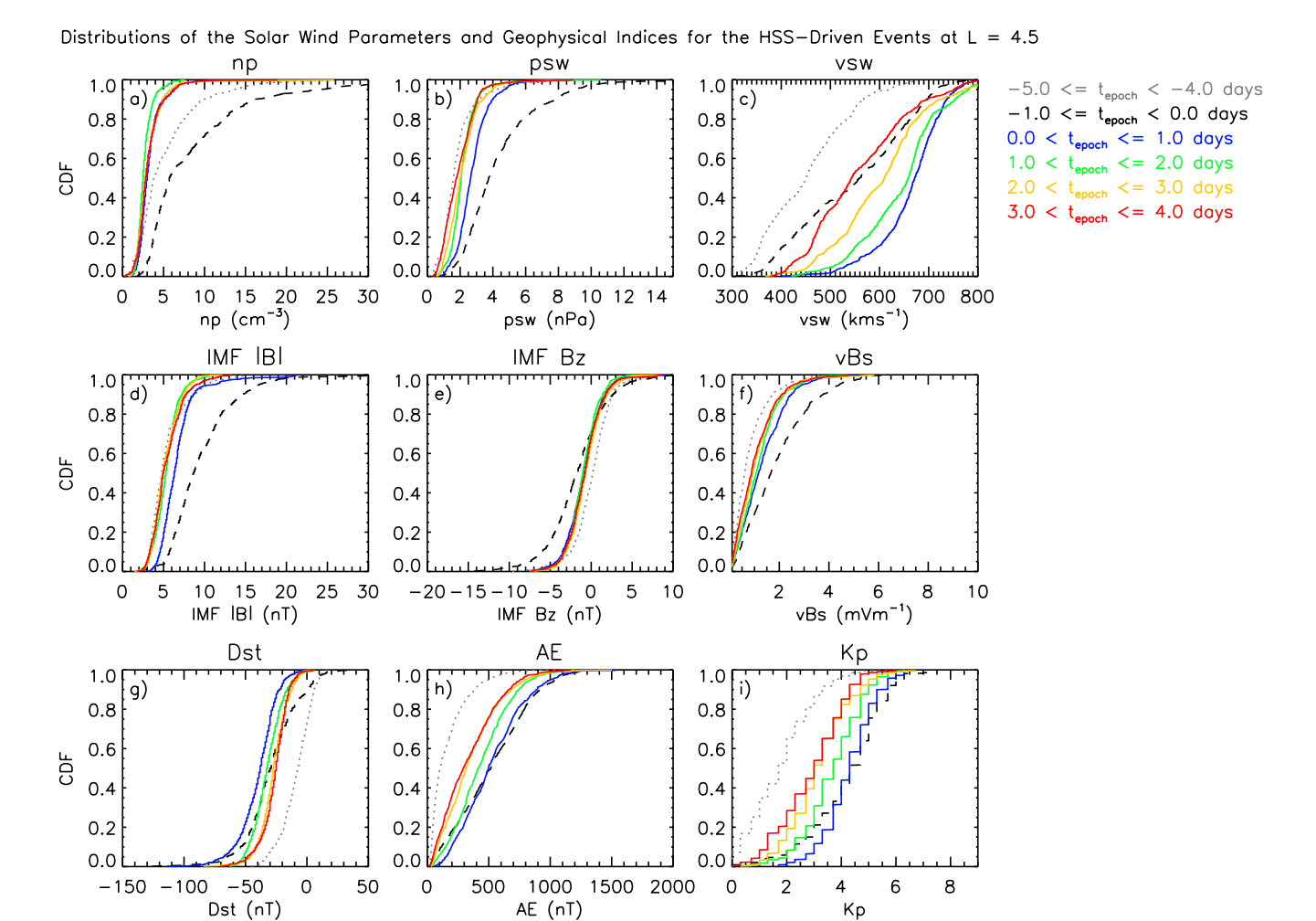


Figure 5.

MEREDITH ET AL. 12 of 28

15427390, 2025, 11, Downloaded

from https://agupubs.onlinelibrary.wiley.com/doi/10.1029/2025SW004633 by NICE, National Institute for Health and Care Excellence, Wiley Online Library on [21/11/2025]. See the Terms



**Figure 6.** Cumulative distribution functions for the solar wind parameters and geophysical indices for the HSS-driven events at L = 4.5 for selected epoch time windows (color-coded). From left to right and top to bottom the panels show (a) the solar wind density; (b) the solar wind pressure; (c) the solar wind velocity; (d) the IMF |B|; (e) IMF  $B_*$ ; (f) the product of the solar wind velocity and the southward component of IMF  $B_*$ ; the Dst index; (h) the AE index; and (i) the Kp index.

The cumulative distributions of the solar wind parameters and geophysical indices determined from the HSS-driven events used in the superposed epoch analysis at L=4.5 are presented for selected epoch time intervals (color-coded) in Figure 6. The separation between the larger values of the solar wind number density (Figure 6a), pressure (Figure 6b) and IMF |B| (Figure 6d) typically observed in the day before zero epoch and the lower values observed following zero epoch are again very clearly visible. As for the CME-driven events, the solar wind number densities following zero epoch (Figure 6a, colored traces) are, for any given percentile, less than the prestorm values (Figure 6a, gray dotted trace) in the bulk of the observations in the 4 days following zero epoch. In contrast, following zero epoch, the distributions of the solar wind pressure (Figure 6b) and IMF |B| (Figure 6d) return to pre-storm values 1–2 days following zero epoch. The distributions of AE (Figure 6h) and Kp (Figure 6i) are again elevated and somewhat similar the day before and following zero epoch. They remain elevated and well above the pre-storm levels, albeit with diminishing values, for any given percentile for the next 3–4 days. IMF  $B_z$  (Figure 6e) is southward in 65%–71% of the observations in the day before and the four days zero epoch.

Figure 5. Statistical properties of the flux of E = 2.0 MeV electrons, the solar wind parameters and geophysical indices in the superposed epoch analysis of the HSS-driven events at L = 4.5. From top to bottom the panels show (a) the BDD IIR electron flux measurements at E = 2.0 MeV; (b) the solar wind pressure; (c) the solar wind number density; (d) the IMF |B|; (e) the IMF  $B_z$ ; (f) the solar wind velocity; (g) the Dst index; (h) the Kp index; and (i) the AE index. In each panel the arithmetic mean, the median and the upper and lower quartiles are coded black, green, red, and blue, respectively. The vertical black dashed lines in (a–i) denote zero epoch. The horizontal dashed line in (a) denotes the limiting flux of E = 2.0 MeV electrons determined from an independent extreme value analysis (Meredith et al., 2023).

MEREDITH ET AL. 13 of 28

#### 3.2. L = 6.5

NS41 typically crossed L=6.5 at magnetic latitudes between 35 and 38°. Here, assuming a dipole field, mirroring electrons would have equatorial pitch angles between 24 and 28°. Larger pitch angles would not be sampled. Shi et al. (2016) recently reported relatively flat relativistic electron pitch angle distributions in the outer radiation belt, both during quiet and active conditions, typically being represented by  $\sin^n(\alpha)$  distribution with n less than 1. This implies that the pitch angle distributions will be relatively flat and that the omnidirectional flux at the equator at L=6.5 could be similar to or a factor of 2 or 3 larger than that measured in GPS orbit, depending on the anisotropy. However, since we do not know the anisotropy, we do not attempt a flux conversion and, in this section, focus on the results at L=6.5 in GPS orbit.

#### 3.2.1. CME-Driven Events

Thirteen of the top fifty E=2.0 MeV electron flux enhancements at L=6.5 were associated with storms driven by coronal mass ejections (Meredith et al., 2024). We excluded the peak flux events of 30 July 2004, 15 November 2004, 21 September 2005, 21 March 2012, 20 October 2012 since they were either preceded or followed by an additional geomagnetic storm, five days either side of zero epoch, leaving us with eight events for the analysis. Six of the CME-driven events at L=6.5 also appear among the fifteen E=2.0 MeV event at L=4.5 and hence are included the superposed epoch analyses at both the higher and lower L shells.

The results of the superposed epoch analysis for the CME-driven events at L=6.5 are presented in Figure 7, in the same format as Figure 1. The key features are presented in the second and third columns of Table 3 and the temporal extent of selected key features are presented in the second, third and fourth columns of Table 4. The solar wind conditions (Figures 7e-7g) are somewhat similar to those observed during the CME-driven storms at L=4.5, albeit the peaks in the solar wind number density (Figure 7f, red trace) and pressure (Figure 7g, red trace) are factors of 1.2 and 1.3 times lower, respectively, than those observed during the CME-driven storms at L=4.5. The Dst (Figure 7g, color-coded), Kp (Figure 7h, color coded) and AE (Figure 7i, black trace) responses are also somewhat similar, the exception being during the recovery phase where the Dst, Kp and AE indices return more quickly to their pre-storm levels, with the Kp index remaining greater than 3 and the AE index remaining above 300 nT for 1.1 days following zero epoch.

In contrast to the solar wind parameters and geophysical indices, major differences can be seen in the electron response. The electron fluxes (Figures 7a–7d) show local maxima 1–2 days prior to zero epoch, reaching minima a few hours after zero epoch. The fluxes then increase at all energies, reaching their maximum values 4 days later. The peak electron flux at  $E=2.0\,\mathrm{MeV}$  is  $5.3\times10^4\,\mathrm{cm^{-2}~s^{-1}~sr^{-1}~MeV^{-1}}$  a factor of 21 lower than that observed at  $L=4.5\,\mathrm{during}$  the CME-driven storms.

The statistical properties of the flux of E=2.0 MeV electrons, the solar wind parameters and geophysical indices in the superposed epoch analysis of the CME-driven events at L=6.5 are shown in Figure 8 in the same format as Figure 2. Prominent features observed in Figure 7 using the mean values are clearly visible in the upper and lower quartiles and median values, including the peaks in the solar wind pressure (Figure 8b) density (Figure 8c) and IMF |B| (Figure 8d) prior to the zero epoch, the minima in the Dst index (Figure 8g) and IMF  $B_z$  (Figure 8e) at or around zero epoch and enhancements in the Kp and AE indices (Figures 8h and 8i respectively). There is a wide spread in the fluxes of E=2.0 MeV electrons both prior to and following zero epoch (Figure 8a), showing the larger variability in the fluxes of the E=2.0 MeV electrons in this region.

The cumulative distributions of the solar wind parameters and geophysical indices determined from the CME-driven events used in the superposed epoch analysis at L=6.5 are presented for selected epoch time intervals (color-coded) in Figure 9. The distributions are somewhat similar to those associated with the CME-driven events at L=4.5. A notable difference is the quicker return to quiet time levels with the distributions of the AE and Kp indices closely resembling the pre-storm distributions 2–3 days following zero epoch.

#### 3.2.2. HSS-Driven Events

The results of the superposed epoch analysis for the thirty seven HSS-driven events at L=6.5 are presented in Figure 10, in the same format as Figure 1. The key features are presented in the fourth and fifth columns of Table 3 and the temporal extent of selected key features are presented in the fifth, sixth and seventh columns of Table 4.

MEREDITH ET AL. 14 of 28

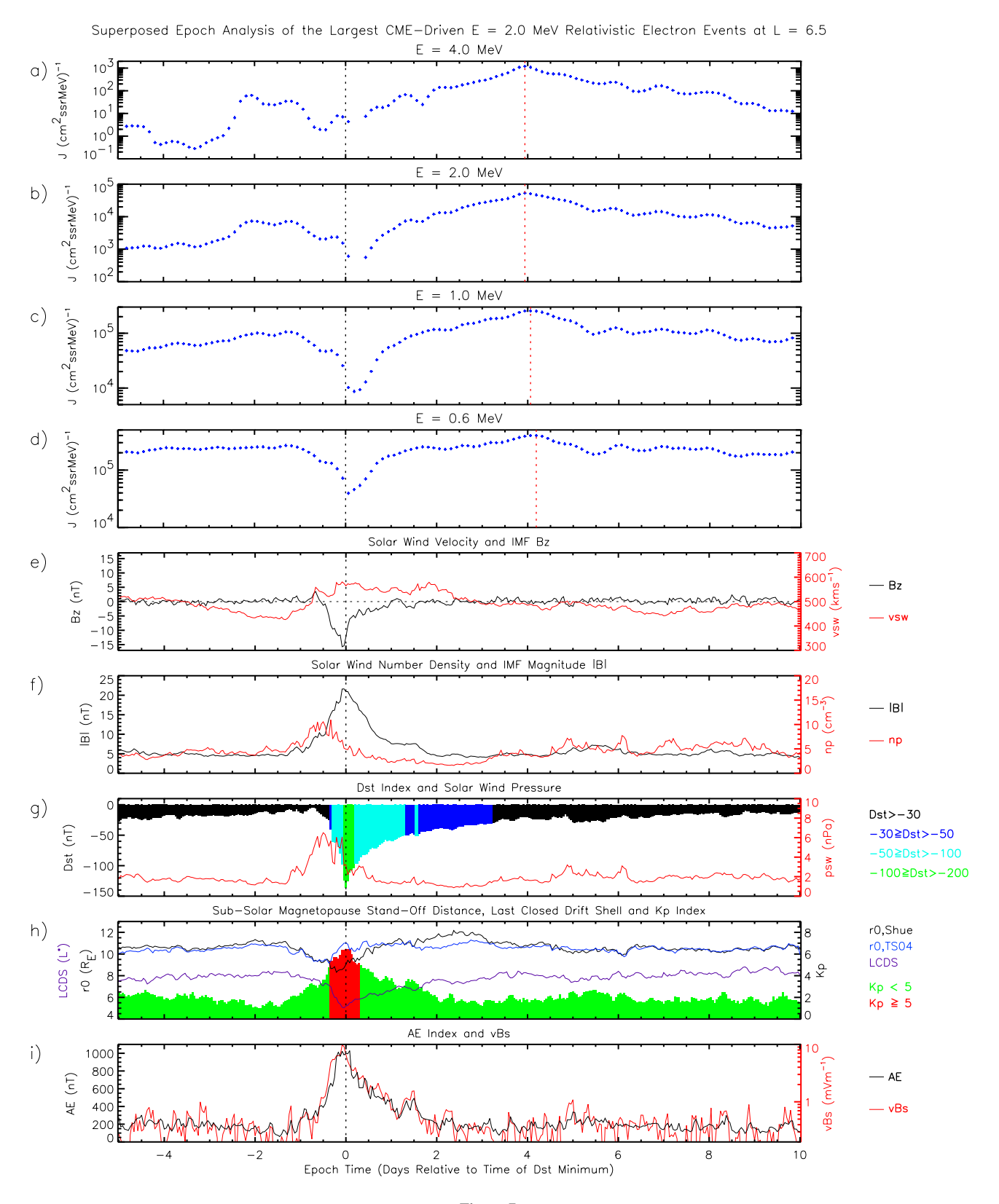


Figure 7.

MEREDITH ET AL. 15 of 28

**Table 3** *Key Features of the Solar Wind Parameters, Geophysical Indices and Electron Fluxes From the Superposed Epoch Analyses for the CME- and HSS-Driven Events at L=6.5* 

	CME-driven events		HSS-driven events		
Parameter	$t_{epoch}$	Value	$t_{epoch}$	Value	
Psw,max	-12 hr	6.5 nPa	-8 hr	4.9 nPa	
$r_{0,TS04,\min}$	−9 hr	$9.2~\mathrm{R}_E$	-8 hr	9.1 R <sub>E</sub>	
$n_{p,\max}$	-8 hr	$11 \text{ cm}^{-3}$	-13 hr	$11 \text{ cm}^{-3}$	
$v_{sw,\max}$	−2 hr	$580 \text{ km s}^{-1}$	+1.5 days	$637 \text{ km s}^{-1}$	
IMF $B_{z,\min}$	−2 hr	-16 nT	−2 hr	−4.3 nT	
IMF $ B _{\text{max}}$	−1 hr	22 nT	−7 hr	10 nT	
LCDS <sub>min</sub>	−1 hr	$L^* = 5.0$	0	$L^* = 6.3$	
$Dst_{\min}$	0	−136 nT	0	−54 nT	
$Kp_{\max}$	+1 hr	6.5	−2 hr	4.8	
$AE_{\text{max}}$	+2 hr	1,029 nT	−1 hr	734 nT	
$J(0.6MeV)_{\rm max}$	+4.2 days	$4.0 \times 10^5 \text{ (cm}^2 \text{ssrMeV})^{-1}$	+4.4 days	$3.4 \times 10^5 \text{ (cm}^2 \text{ssrMeV)}^{-1}$	
$J(1.0MeV)_{\text{max}}$	+4.1 days	$2.6 \times 10^5 \text{ (cm}^2 \text{ssrMeV})^{-1}$	+4.6 days	$1.8 \times 10^5 \text{ (cm}^2 \text{ssrMeV)}^{-1}$	
$J(2.0MeV)_{\rm max}$	+3.9 days	$5.3 \times 10^4 \text{ (cm}^2 \text{ssrMeV})^{-1}$	+4.7 days	$2.2 \times 10^4 \text{ (cm}^2 \text{ssrMeV})^{-1}$	
$J(4.0MeV)_{\text{max}}$	+3.9 days	$1.2 \times 10^3 \text{ (cm}^2 \text{ssrMeV})^{-1}$	+5.9 days	$2.1 \times 10^2 \text{ (cm}^2 \text{ssrMeV})^{-1}$	

Fifteen of the thirty-seven HSS-driven events at L = 6.5 also appear among the thirty E = 2.0 MeV events at L = 4.5 and hence are included the superposed epoch analyses at both the higher and lower L shells.

The behavior of the solar wind number density (Figure 10f, red trace), pressure (Figure 10g, red trace) and IMF |B| (Figure 10f, black trace) are somewhat similar to those observed during the HSS-driven storms at L=4.5. However, the solar wind speed (Figure 10e, red trace) is slightly weaker and less sustained for the events at L=6.5. In this case, the solar wind speed starts increasing 1 day prior to zero epoch, maximizing around 640 km s<sup>-1</sup> for  $0.5 < t_{epoch} < 1.5$  days prior to gradually falling below 500 km s<sup>-1</sup> 4.2 days following zero epoch. During this interval, the solar wind speed remains above 550 km s<sup>-1</sup> from 3 hr before zero epoch to 3.1 days afterward. The Dst (Figure 10g, color-coded), Kp (Figure 10h, color coded) and AE (Figure 10i, black trace) responses are also somewhat similar, the exception being during the recovery phase when the Dst, Kp, and AE indices return more quickly to their pre-storm levels, with the Kp index remaining above 3 and the AE index remaining above 300 nT for 1.5 and 1.8 days following zero epoch respectively.

Very different electron responses (Figures 10a–10d) are seen at L=6.5. The major difference is the behavior of the fluxes prior to zero epoch. In this region the fluxes tend to increase from 5 days prior to zero epoch and reach local maxima around 3 days prior to zero epoch. The fluxes are then observed to fall at all energies, minimizing around zero epoch and subsequently rising to maxima about 4.5 days after zero epoch. The flux of E=2.0 MeV electrons peaks at  $2.2 \times 10^4$  cm<sup>-2</sup> s<sup>-1</sup> sr<sup>-1</sup> MeV<sup>-1</sup> a factor of 40 lower than that observed at L=4.5 during HSS-driven storms and a factor of 2.4 lower than that observed at L=6.5 during CME-driven storms.

The statistical properties of the flux of E = 2.0 MeV electrons, the solar wind parameters and geophysical indices in the superposed epoch analysis of the HSS-driven events at L = 6.5 are shown in Figure 11 in the same format as Figure 2. Prominent features observed in Figure 10 using the mean values are clearly visible in the upper and lower quartiles and median values, including the peaks in the solar wind pressure (Figure 11b) density

Figure 7. Superposed epoch analysis for the CME-driven events at L=6.5. From top to bottom the panels show (a–d) the BDD IIR electron flux measurements at E=4.0, 2.0, 1.0 and 0.6 MeV respectively; (e) the solar wind velocity (red trace) and the IMF  $B_z$  (black trace); (f) the solar wind number density (red trace) and the IMF |B| (black trace); (g) the Dst index (color-coded) and solar wind pressure (red trace); (h) the Kp index (color-coded) and the Shue et al. (1998) and TS04 sub-solar magnetopause positions (black and blue traces respectively) and the TS04 last closed drift shell (purple trace); (i) the AE index (black trace) and the product of the solar wind velocity and the southward component of IMF  $B_z$  (red trace). The vertical black dashed lines in (a–i) denote zero epoch and the vertical red dashed lines in (a–d) mark the time of the peak electron flux at the selected energy.

MEREDITH ET AL. 16 of 28

**Table 4**Duration of Selected Solar Wind Parameters and Geophysical Indices With Respect to Set Levels at L = 6.5

		CME-driven events			HSS-driven events		
Parameter	$t_{begin}$	$t_{end}$	Duration	$t_{begin}$	$t_{end}$	Duration	
$n_p < 4 \text{ cm}^{-3}$	+4 hr	+3.4 days	3.2 days	+12 hr	+4.9 days	4.4 days	
$v_{sw} > 550 \text{ km s}^{-1}$	−5 hr	+9 hr	14 hr	−3 hr	+3.1 days	3.2 days	
Dst < -30  nT	-8 hr	+3.2 days	3.5 days	-4 hr	+15 hr	19 hr	
AE > 300  nT	-14 hr	+1.1 days	1.7 days	-15 hr	+1.8 days	2.4 days	
Kp > 3	-14 hr	+1.1 days	1.7 days	-14 hr	+1.5 days	2.1 days	

(Figure 11c) and IMF |B| (Figure 11d) prior to the zero epoch and the minima in the Dst index (Figure 11g) and IMF  $B_z$  (Figure 11e) at or around zero epoch. The solar wind speed is again more tightly constrained than for the CME events with even the lower quartile exceeding 500 km s<sup>-1</sup> for 2.5 days (Figure 11f). Enhancements in the Kp and AE indices in Figure 10 are also seen prior to and following zero epoch in the upper and lower quartiles and median values (Figures 11h and 11i respectively). There is a very wide spread in the fluxes of E = 2.0 MeV electrons prior to zero epoch (Figure 11a), of the order of a factor of 100, caused by differences in the pre-storm flux levels. The post-storm maxima are more tightly constrained but with more variability than that observed at E = 4.5.

The cumulative distributions of the solar wind parameters and geophysical indices determined from the HSS-driven events used in the superposed epoch analysis at L=6.5 are presented for selected epoch time intervals (color-coded) in Figure 12. The distributions are somewhat similar to those associated with the HSS-driven events at L=4.5. Notable differences include smaller solar wind velocities and reduced geomagnetic activity as monitored by the AE and Kp indices.

#### 4. Discussion

Our analysis reveals the solar wind and geomagnetic conditions that are associated with the largest relativistic electron flux enhancements in GPS orbit both during CME- and HSS-driven storms. The work reveals that while the relativistic electron fluxes tend to peak several days following the storm-time *Dst* minimum, there are many signatures in the solar wind and geomagnetic indices that occur before the flux peaks and may be used by spacecraft operators and engineers to help interpret the development of a storm while it is in progress and, hence, assess the likelihood of a significant relativistic electron flux enhancement before it occurs and possibly take some precautionary measures in an attempt to mitigate the damage to satellites.

The CME-driven and HSS-driven storms leading to the largest relativistic electron fluxes at L=4.5 are both associated with enhancements in the solar wind number density, pressure, and IMF |B| prior to zero epoch. However, the enhancements in the pressure, density and IMF |B| are stronger during the CME-driven events being factors of 1.2–1.6 times larger than those associated with the HSS-driven storms. Significantly, the minimum IMF  $B_z$  and the minimum Dst are approximately three and two times more negative, respectively, during the CME-driven storms. In contrast, the solar wind speed is predominantly higher and more sustained during the HSS-driven events. The recovery phases are associated with weakly southward IMF  $B_z$  and elevated substorm activity as monitored by the AE index, with AE > 300 nT for 2.0 and 2.5 days following zero epoch for the CME-driven and HSS-driven events respectively. These solar wind and magnetospheric conditions lead to the build up of the largest relativistic electron fluxes in this region. The peak values are slightly larger during the CME-driven storms, being factors of 1.2–1.3 larger at energies from E=0.6–2.0 MeV and a factor of 1.5 larger at E=4.0 MeV. The rise-times are energy dependent, ranging from 1.6–1.9 days at E=0.6 MeV to 2.9–3.8 days at E=4.0 MeV for the HSS- and CME-driven events respectively.

The CME-driven and HSS-driven storms leading to the largest relativistic electron fluxes at L=6.5 are also both associated with enhancements in the solar wind number density, pressure, and IMF |B| prior to zero epoch. The enhancements in the solar wind number density are similar for the two classes of events and similar to that observed during the HSS-driven storms at L=4.5. In contrast, the peaks in solar wind pressure, IMF |B|, the southward component of the IMF, the absolute values of Dst and AE are stronger during the CME-driven storms,

MEREDITH ET AL. 17 of 28

15427390, 2025, 11, Downloaded from https://gupubs.onlinebitary.wiley.com/doi/10.1029/2025SW004033 by NICE, National Institute for Health and Care Excellence, Wiley Online Library on [21/11/2025]. See the Terms and Conditions (https://onlinebitary.wiley.com/doi/ninebitar

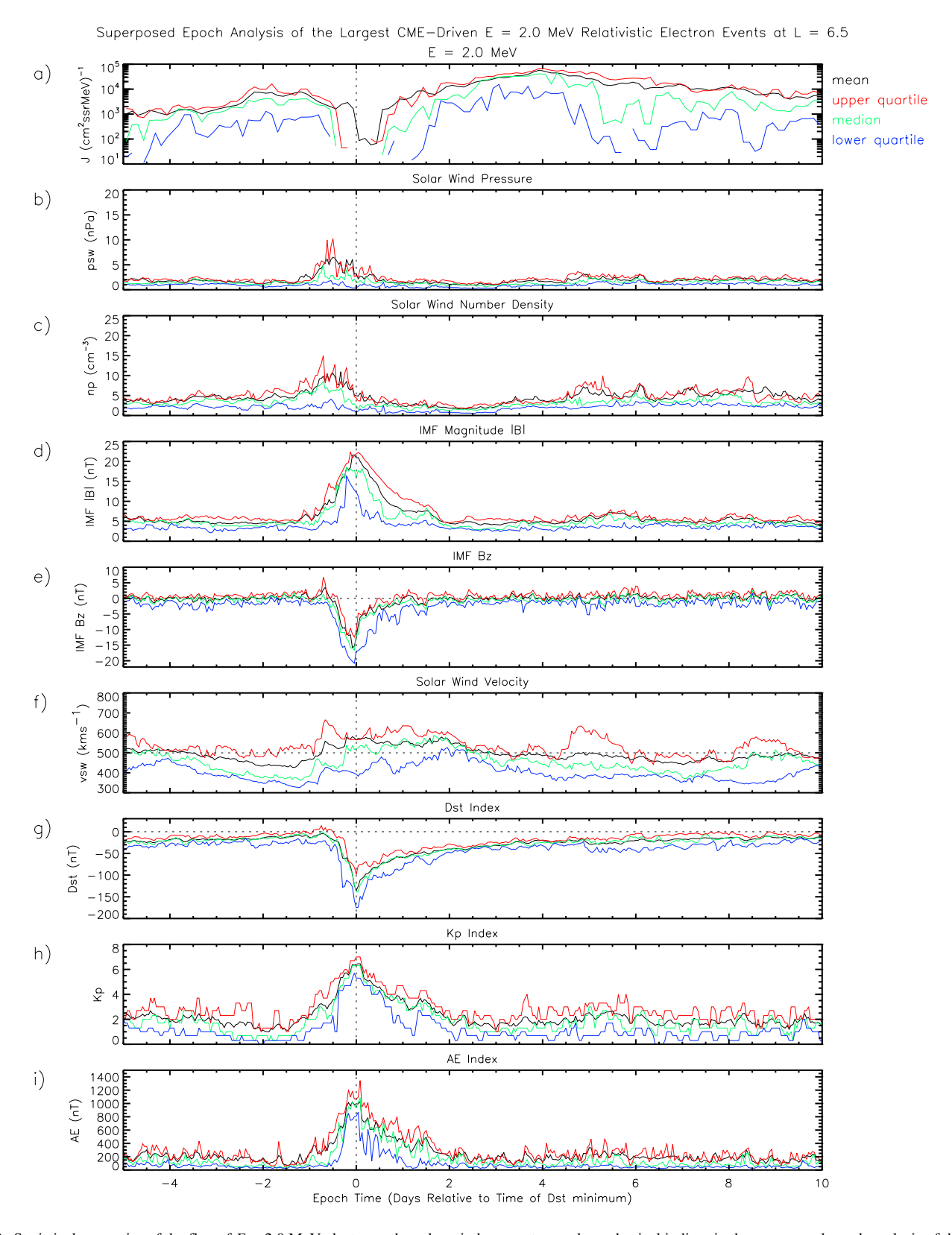


Figure 8. Statistical properties of the flux of E = 2.0 MeV electrons, the solar wind parameters and geophysical indices in the superposed epoch analysis of the CME-driven events at E = 6.5. From top to bottom the panels show (a) the BDD IIR electron flux measurements at E = 2.0 MeV; (b) the solar wind pressure; (c) the solar wind number density; (d) the IMF |B|; (e) the IMF  $B_z$ ; (f) the solar wind velocity; (g) the Dst index; (h) the Kp index; and (i) the AE index. In each panel the arithmetic mean, the median and the upper and lower quartiles are coded black, green, red, and blue, respectively. The vertical black dashed lines in (a-i) denote zero epoch.

MEREDITH ET AL. 18 of 28

from https://agupubs.onlinelibrary.wiley.com/doi/10.1029/2025SW004633 by NICE, National Institute for Health

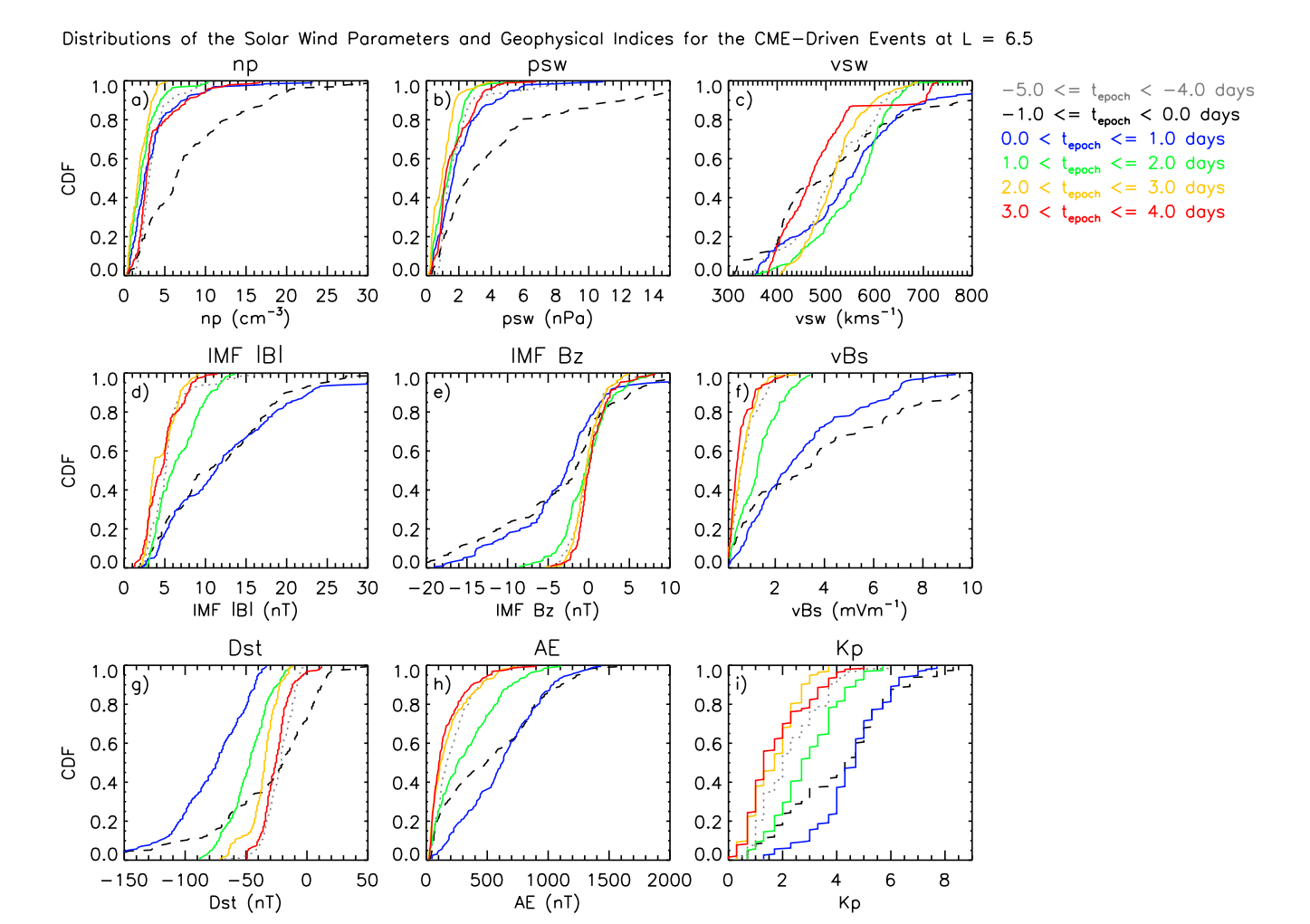


Figure 9. Cumulative distribution functions for the solar wind parameters and geophysical indices for the CME-driven events at L = 6.5 for selected epoch time windows (color-coded). From left to right and top to bottom the panels show (a) the solar wind density; (b) the solar wind pressure; (c) the solar wind velocity; (d) the IMF |B|; (e) the IMF  $B_r$ ; (f) the product of the solar wind velocity and the southward component of IMF  $B_r$ ; (g) the Dst index; (h) the AE index; and (i) the Kp index.

with peak values factors of 1.3, 2.2, 3.7, 2.5, and 1.4 larger, respectively, than those observed during the HSS-driven storms. The recovery phases are associated with weakly southward IMF  $B_z$  and associated elevated substorm activity as monitored by the AE index, with AE > 300 nT for 1.1 and 1.8 days following zero epoch for the CME-driven and HSS-driven events respectively. These solar wind and magnetospheric conditions lead to the build up of the largest relativistic electron fluxes in this region. The peak values are largest during the CME-driven events, being factors of 1.4, 2.4, and 5.7 larger than the HSS-driven events at E = 1.0, 2.0, and 4.0 MeV respectively. The rise-times show little energy dependence and are remarkably similar during the CME- and HSS-driven events.

Our results show that strong relativistic electron flux enhancements are associated with enhanced number densities and solar wind pressures in the day prior to zero epoch and lower values following zero epoch. This is consistent with Pinto et al. (2018) who found similar trends during relativistic electron enhancement events. In particular, our observations show that the solar wind densities fall predominantly below  $4 \text{ cm}^{-3}$  for  $\sim 3$  days and  $\sim 5$  days following zero epoch for the CME- and HSS-driven events respectively. Interestingly, Pinto et al. (2018) found that during persistent relativistic electron depletion events the number densities and pressures tended to remain elevated both prior to and following the event onset. This suggests that it is the lower densities and pressures following zero epoch that enable electron enhancement events to proceed.

The fluxes at L = 4.5 are relatively flat in the 5 day period prior to zero epoch. In contrast, peaks in the electron flux are observed at L = 6.5 prior to zero epoch and these are especially evident during the high speed streams,

MEREDITH ET AL. 19 of 28

15427390, 2025, 11, Downloaded from https://agupubs.onlinelibrary.wikey.com/doi/10.1092/025SW004633 by NICE, National Institute for Health and Care Excellence, Wiley Online Library on [21/11/2025]. See the Terms and Conditions (https://oilinelibrary.wikey.com/ems-and-conditions) on Wiley Online Library for rules of use; 0, Aarticle sar governed by the applicable the Cerems and Conditions (https://oilinelibrary.wikey.com/ems-and-conditions) on Wiley Online Library for rules of use; 0, Aarticle sar governed by the applicable the Cerems and Conditions (https://oilinelibrary.wikey.com/ems-and-conditions) on Wiley Online Library for rules of use; 0, Aarticle sar governed by the applicable the Cerems and Conditions (https://oilinelibrary.wikey.com/ems-and-conditions) on Wiley Online Library for rules of use; 0, Aarticle sar governed by the applicable the Cerems and Conditions (https://oilinelibrary.wikey.com/ems-and-conditions) on Wiley Online Library for rules of use; 0, Aarticle sar governed by the applicable the Cerems and Conditions (https://oilinelibrary.wikey.com/ems-and-conditions) on Wiley Online Library for rules of use; 0, Aarticle sar governed by the applicable the Cerems and Conditions (https://oilinelibrary.wikey.com/ems-and-conditions) on Wiley Online Library for rules of use; 0, Aarticle sar governed by the applicable the conditions (https://oilinelibrary.wikey.com/ems-and-conditions) on the conditions (https://oilinelibrary.wikey.com/ems-and-co

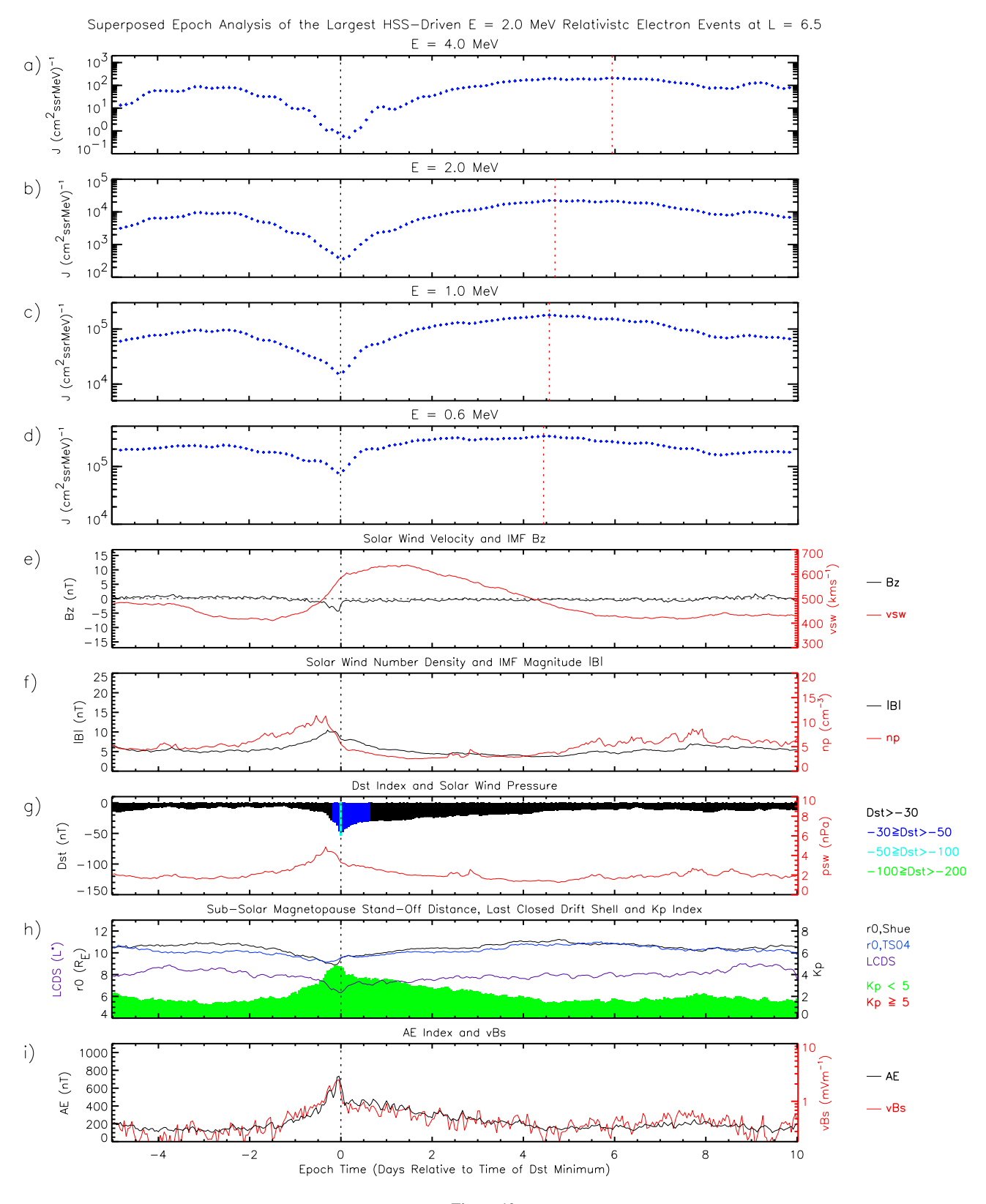


Figure 10.

MEREDITH ET AL. 20 of 28

where, for example, the flux of E = 2.0 MeV electrons rises from 5 days prior to zero epoch, peaks at 3.1 days prior to zero epoch and reaches a minimum near zero epoch, before rising to the post-storm maximum 4.7 days later. There are thus, on average, 7.8 days between the pre- and post-storm flux maxima. The flux peak prior to zero epoch at L = 6.5 is due to the strength and frequency of the high speed stream driven storms. Strong high speed streams affect the relativistic electron dynamics at L = 4.5 and L = 6.5, whereas weaker high speed streams are only effective further out. This is illustrated in Figure 13 which shows the behavior of the relativistic electron fluxes, solar wind parameters and geophysical indices for May 2016, during the declining phase of solar cycle 24 (Sawadogo et al., 2024). During this period there are four HSS-driven events, all resulting in flux enhancements at the largest values of L, where, for example, peaks in the flux of E = 2.0 MeV electrons are seen on 5, 12, 19, and 27 May. Further in, at L = 4.5, there are two peaks in the flux of E = 2.0 MeV electrons on 4 and 11 May with no response evident to the two weaker HSS-driven events later in the month. We find that there are 14 HSS-driven events at L = 6.5 that are associated with pre-storm flux peaks occurring 7–9 days prior to the event maximum, all associated with an earlier high speed stream. We conclude that the pre-zero epoch peak that occurs in the superposed epoch analysis at L = 6.5 is due to previous high speed streams, occurring 7–9 days prior to zero epoch.

The minimum in the relativistic electron fluxes observed during the high speed stream events at L = 6.5 is due to enhanced magnetopause shadowing (e.g., Turner et al., 2012) caused by the inward movement of the last closed drift shell which reaches  $L^* = 6.3$  at zero epoch. This is even more evident in the CME-driven events in this region. Due to the stronger solar wind drivers the last closed drift shell moves in to  $L^* = 5.1$  1 hr prior to zero epoch resulting in large flux drop-outs abruptly following zero epoch. Further in, at L=4.5 there are no strong minima or flux dropouts near zero epoch, since this region is well inside the last-closed drift shell, during both the HSS- and CME-driven events.

Our superposed epoch analysis shows that the strongest flux enhancements are associated with prolonged substorm activity as monitored by the AE index, with the AE index exceeding 300 nT for 2.0 and 2.5 days following zero epoch for the CME- and HSS-driven storms at L = 4.5 and for 1.1 and 1.8 days following zero epoch for the CME- and HSS-driven storms at L = 6.5. Such periods are associated with enhanced whistler mode chorus wave activity (Agapitov et al., 2018; Li et al., 2009; Meredith et al., 2001, 2012, 2020; Miyoshi et al., 2013), enhanced fluxes of seed electrons (Hua et al., 2023; Jaynes et al., 2015; Meredith et al., 2003) and the gradual acceleration of seed electrons to relativistic energies driven by the enhanced whistler mode chorus wave activity (Horne et al., 2005; Hua, Bortnik, & Ma, 2022; Hua et al., 2023; Jaynes et al., 2015; Meredith et al., 2003; Thorne et al., 2013; Tu et al., 2014). The results are also consistent with recent studies which have shown that storm-time relativistic electron flux enhancements are associated with periods of enhanced substorm activity as monitored by the time integrated AL index (Hua & Bortnik, 2024; Hua, Bortnik, Chu, et al., 2022; Hua et al., 2023).

Meredith et al. (2023) used extreme value analysis to show that the fluxes of E = 2.0 MeV electrons at L = 4.5tend to a limiting value of  $2.2 \times 10^6$  cm<sup>-2</sup> s<sup>-1</sup> sr<sup>-1</sup> MeV<sup>-1</sup>. The upper and lower quartiles of the flux maxima in the superposed epoch analysis range from a factor of 2-4 below this limiting flux, for both the CME- and HSSdriven storms (Figures 2a and 5a). This suggests that E = 2.0 MeV electron fluxes can be driven toward their limiting value by both CME- and HSS-driven storms. Further out, at L = 6.5, the fluxes of E = 2.0 MeV electrons were not found to tend to a limiting value (Meredith et al., 2023), consistent with the wider range of flux maxima observed in the superposed epoch analyses in this region (Figures 8a and 11a).

The behavior of the AE index is remarkably well-correlated with the behavior of the product of the logarithm of the solar wind speed and the southward component of IMF, vBs, for the largest E = 2.0 MeV electron fluxes at L = 4.5 and 6.5, both for CME- and HSS-driven storms. This demonstrates the importance of enhanced substorm activity as monitored by AE which is itself related to the energy input into the magnetosphere as parameterized by the interplanetary electric field Ey = vBs.

Figure 10. Superposed epoch analysis for the HSS-driven events at L = 6.5. From top to bottom the panels show (a–d) the BDD IIR electron flux measurements at E = 4.0, 2.0, 1.0 and 0.6 MeV respectively; (e) the solar wind velocity (red trace) and the IMF B<sub>x</sub> (black trace); (f) the solar wind number density (red trace) and the IMF |B| (black trace); (g) the Dst index (color-coded) and solar wind pressure (red trace); (h) the Kp index (color-coded) and the Shue et al. (1998) and TS04 sub-solar magnetopause positions (black and blue traces respectively) and the TS04 last closed drift shell (purple trace); (i) the AE index (black trace) and the product of the solar wind velocity and the southward component of IMF  $B_z$  (red trace). The vertical black dashed lines in (a-i) denote zero epoch and the vertical red dashed lines in (a-d) mark the time of the peak electron flux at the selected energy.

MEREDITH ET AL. 21 of 28

15427390, 2025, 11, Downloaded from https://gupubs.onlinelibrary.wiley.com/e/oi/10.1092/025SW004633 by NICE, National Institute for Health and Care Excellence, Wiley Online Library on [21/11/2025]. See the Terms and Conditions (https://oinnleibrary.wiley.com/ems-and-conditions) on Wiley Online Library or rules of use, e) A articles are governed by the applicable here.

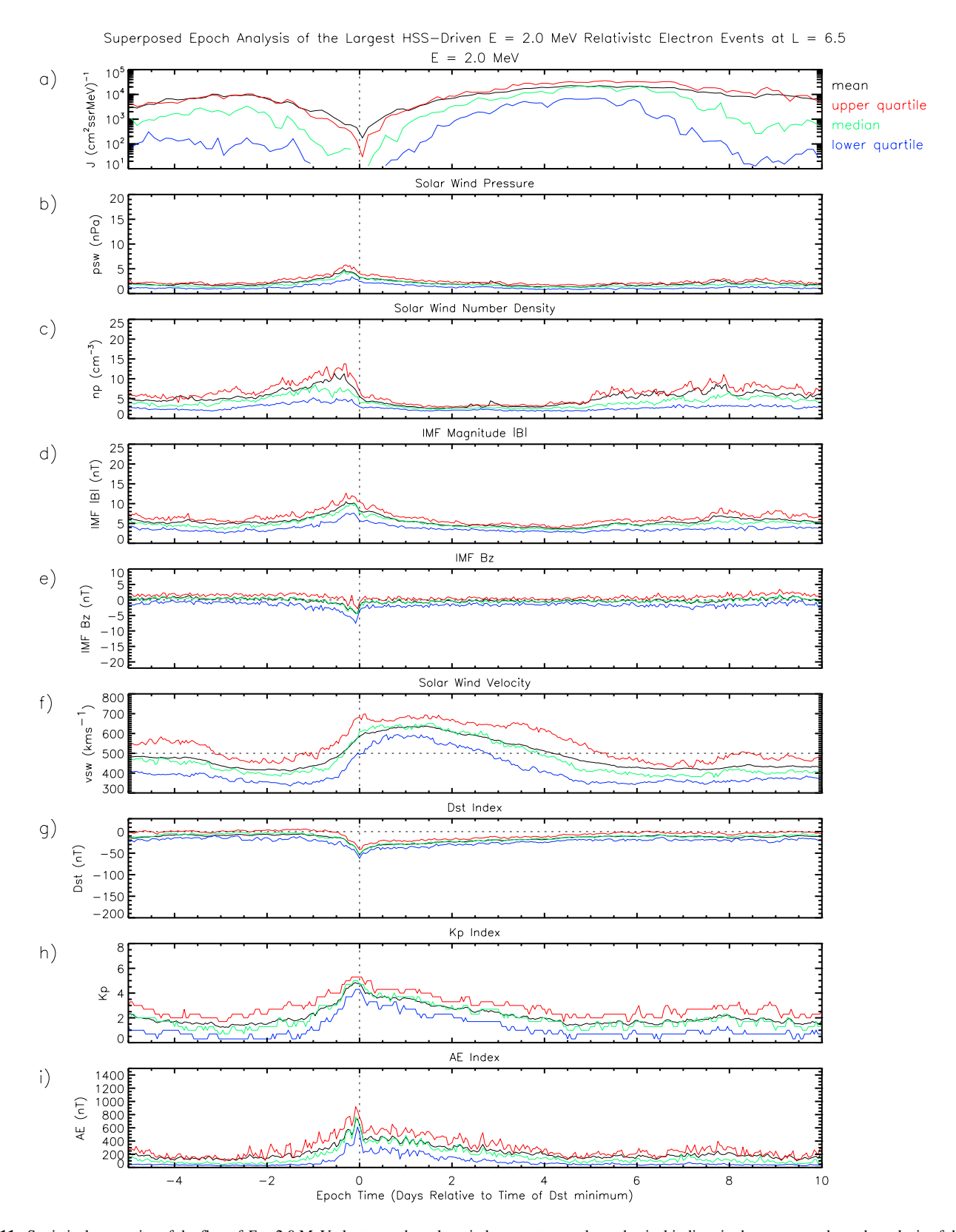


Figure 11. Statistical properties of the flux of E = 2.0 MeV electrons, the solar wind parameters and geophysical indices in the superposed epoch analysis of the HSS-driven events at E = 6.5. From top to bottom the panels show (a) the BDD IIR electron flux measurements at E = 2.0 MeV; (b) the solar wind pressure; (c) the solar wind number density; (d) the IMF |B|; (e) the IMF  $B_z$ ; (f) the solar wind velocity; (g) the Dst index; (h) the Kp index; and (i) the AE index. In each panel the arithmetic mean, the median and the upper and lower quartiles are coded black, green, red, and blue, respectively. The vertical black dashed lines in (a-i) denote zero epoch.

MEREDITH ET AL. 22 of 28

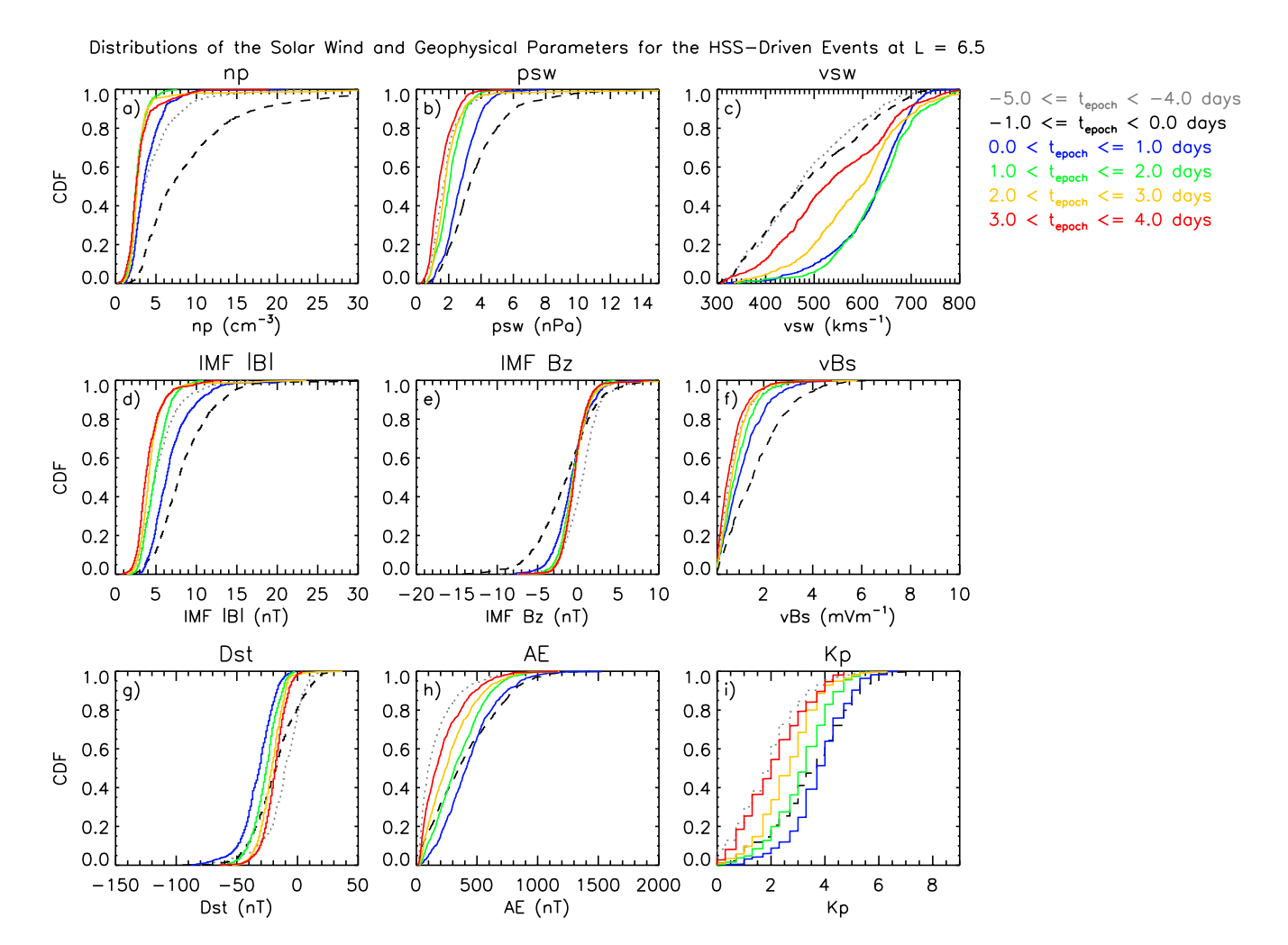


Figure 12. Cumulative distribution functions for the solar wind parameters and geophysical indices for the HSS-driven events at L = 6.5 for selected epoch time windows (color-coded). From left to right and top to bottom the panels show (a) the solar wind density; (b) the solar wind pressure; (c) the solar wind velocity; (d) the IMF |B|; (e) the IMF  $B_z$ ; (f) the product of the solar wind velocity and the southward component of IMF  $B_z$ ; (g) the Dst index; (h) the AE index; and (i) the Kp index.

The data used in this analysis comes from the US GPS satellite NS41 at a cadence of roughly 8 measurements for any given *L* shell and energy per day. The superposed epoch analysis at a 3 hr time resolution, using 6 hr bins, has approximately twice the number of data points per bin as the number of events and is sufficient for the current study. Further analysis, involving additional GPS satellites, would improve the statistics and enable the investigation to be conducted at a higher time resolution, but are beyond the scope of this study.

Away from the Dst minimum the separation between sub-solar magnetopause stand-off distance, as determined by the model of Shue et al. (1998),  $r_{0,Shue}$ , and the last closed drift shell, LCDS, remains roughly constant. This changes around the Dst minimum, when  $r_{0,Shue}$  begins to decrease slowly prior to the minimum, and recovers rapidly afterward, whereas the LCDS position decreases more rapidly shortly before the minimum, and recovers much more slowly, most clearly seen during the CME-driven events in Figures 1h and 7h. This mirrors the behavior of their primary drivers.  $r_{0,Shue}$  is driven by the solar wind pressure and IMF  $B_z$ , which both peak prior to the Dst minimum and drop back rapidly afterward.  $L^*$ , and thus the LCDS, is determined by the flux enclosed by a drift orbit (Roederer, 1967), which is strongly affected by the strength of the ring current, represented by Dst in the TS04 model. Like the LCDS position, the Dst index drops rapidly prior to the Dst minimum and recovers more slowly than the solar wind pressure or IMF  $B_z$ . The same effect is seen to a lesser extent in the HSS-driven events in Figures 4h and 10h.

This study also gives us the opportunity to compare the behavior of the sub-solar magnetopause stand-off distance as predicted by the Shue et al. (1998) model,  $r_{0.Shue}$ , and as determined using the TS04 magnetic field model,

MEREDITH ET AL. 23 of 28

15427390, 2025, 11, Downloaded from https://agupubs.onlinelibrary.wiley.com/doi/10.1029/2025SW004633 by NICE, National Institute for Health and Care Excellence, Wiley Online Library on [21/11/2025]. See the Terms and Conditions (https://onlinelibrary.wiley.com/doi/10.1029/2025SW004633 by NICE, National Institute for Health and Care Excellence, Wiley Online Library on [21/11/2025]. See the Terms and Conditions (https://onlinelibrary.wiley.com/doi/10.1029/2025SW004633 by NICE, National Institute for Health and Care Excellence, Wiley Online Library on [21/11/2025]. See the Terms and Conditions (https://onlinelibrary.wiley.com/doi/10.1029/2025SW004633 by NICE, National Institute for Health and Care Excellence, Wiley Online Library on [21/11/2025]. See the Terms and Conditions (https://onlinelibrary.wiley.com/doi/10.1029/2025SW004633 by NICE, National Institute for Health and Care Excellence, Wiley Online Library on [21/11/2025]. See the Terms and Conditions (https://onlinelibrary.wiley.com/doi/10.1029/2025SW004633 by NICE, National Institute for Health and Care Excellence, Wiley Online Library on [21/11/2025]. See the Terms and Conditions (https://onlinelibrary.wiley.com/doi/10.1029/2025SW004633 by NICE, National Institute for Health and Care Excellence, Wiley Online Library on [21/11/2025]. See the Terms and Conditions (https://onlinelibrary.wiley.com/doi/10.1029/2025SW00463) by NICE, National Institute for Health and Care Excellence, Wiley Online Library on [21/11/2025]. See the Terms and Conditions (https://onlinelibrary.wiley.com/doi/10.1029/2025SW00463) by NICE, National Institute for Health and Care Excellence, Wiley Online Library on [21/11/2025]. See the Terms and Conditions (https://onlinelibrary.wiley.com/doi/10.1029/2025SW00463) by NICE, National Institute for Health and Care Excellence, Wiley Online Library on [21/11/2025]. See the Terms and Care Excellence (https://onlinelibrary.wiley.com/doi/10.1029/2025SW00463) by NICE, National Institute for Health and Care Excellence (https://onlinelibrary.wiley.co

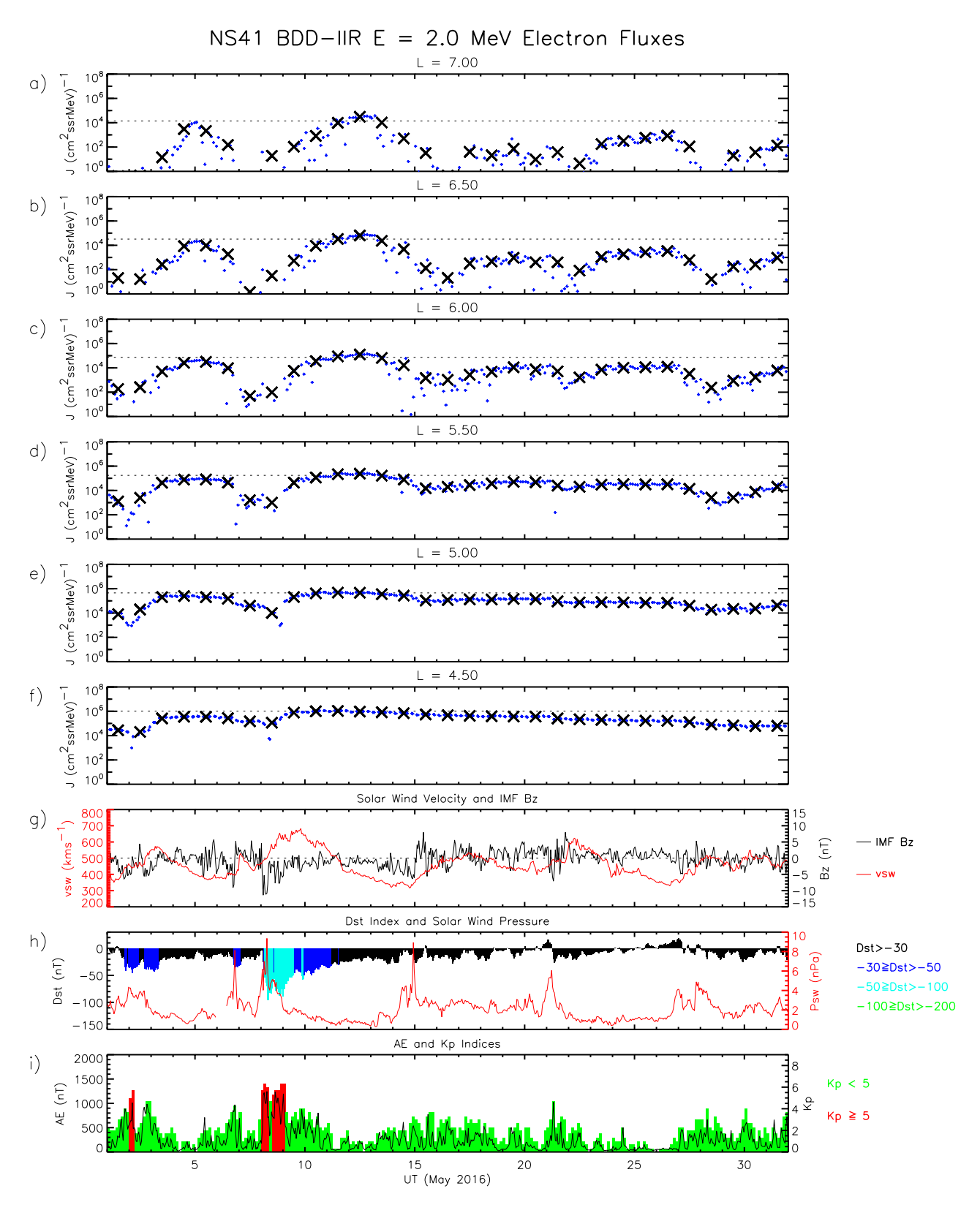


**Figure 13.** Summary plot showing the behavior of the relativistic electron fluxes, solar wind conditions and geophysical parameters for May 2016. From top to bottom, the panels show (a–f) the BDD IIR E = 2.0 MeV electron flux measurements at L = 7.0, 6.5, 6.0, 5.5, 5.0 and 4.5 respectively; (g) the solar wind velocity (red trace) and the IMF  $B_z$  (black trace); (h) the *Dst* index (color-coded) and solar wind pressure (red trace); and (i) the Kp index (color-coded) and the AE index (black trace).

MEREDITH ET AL. 24 of 28

 $r_{0,TS04}$ . Most of the time  $r_{0,TS04}$  is about 0.5–1 R<sub>E</sub> closer to the Earth than  $r_{0,Shue}$ . However, there are large differences near zero epoch for the CME-driven storms with  $r_{0,TS04}$  exceeding  $r_{0,Shue}$  by as much as  $\sim 2R_E$  (Figures 1h and 7h).  $r_{0,TS04}$  is determined using a version of the Shue et al. (1998) magnetopause model which is averaged over IMF  $B_z$ , and depends only on the solar wind pressure (Tsyganenko et al., 2003). Thus, during quiet times,  $r_{0,TS04}$  will be less than  $r_{0,Shue}$  and may be significantly larger during strong southward IMF  $B_z$  as observed.

#### 5. Conclusions

We have conducted superposed epoch analyses of the top fifty E = 2.0 MeV electron flux events at L = 4.5 and L = 6.5, sorting them by solar wind driver, to determine the solar wind and geomagnetic conditions that lead to the largest relativistic electron fluxes in GPS orbit. Our principle results are as follows:

- The CME-driven events are associated with negative excursions of IMF  $B_z$  with minimum values of  $\sim$ -14 nT two hours prior to zero epoch and strong Dst minima, reaching  $\sim$ -130 nT at zero epoch.
- The HSS-driven storms are associated with smaller negative excursions of IMF  $B_z$  with minimum values of  $\sim$ -4 nT one to two hours prior to zero epoch and moderate Dst minima, reaching  $\sim$ -60 nT at zero epoch.
- Both the CME- and HSS-driven events are associated with enhancements in the solar wind number density prior to zero epoch, followed by reductions, with low solar wind densities ( $n_p < 4 \text{ cm}^{-3}$ ) for  $\sim 3$  days to  $\sim 5$  days following zero epoch for the CME- and HSS-driven events respectively.
- Following zero epoch, the CME-driven events are associated with weakly southward IMF  $B_z$  for ~3 days and enhanced substorm activity with AE greater than 300 nT for 1.1–2.0 days.
- Following zero epoch, the HSS-driven events are associated with weakly southward IMF  $B_z$  for ~7 days and enhanced substorm activity with AE greater than 300 nT for 1.8–2.5 days.
- The flux of E = 2.0 MeV electrons associated with the CME-driven storms at L = 4.5 peaks 3.8 days following zero epoch at  $1.1 \times 10^6$  cm<sup>-2</sup> s<sup>-1</sup> sr<sup>-1</sup> MeV<sup>-1</sup>. Further out, at L = 6.5 the E = 2.0 MeV fluxes peak 3.9 days following zero epoch and are a factor of 21 lower.
- The flux of E = 2.0 MeV electrons associated with the HSS-driven storms at L = 4.5 peaks 2.8 days following zero epoch at  $8.8 \times 10^5$  cm<sup>-2</sup> s<sup>-1</sup> sr<sup>-1</sup> MeV<sup>-1</sup>. Further out, at L = 6.5 the E = 2.0 MeV fluxes peak 4.7 days following zero epoch and are a factor of 40 lower.
- The peak E = 2.0 MeV fluxes associated with the CME-driven storms at L = 4.5 and L = 6.5 are factors of 1.3 and 2.4 larger than those associated with the HSS-driven storms.

These results can be used by satellite operators and engineers to assess the likelihood of significant increases in the fluxes of relativistic electrons based on the evolution of the solar wind parameters and geophysical conditions, enabling them to take appropriate precautionary measures if required.

#### **Conflict of Interest**

The authors declare no conflicts of interest relevant to this study.

#### **Data Availability Statement**

The data used in this study is publicly available from https://www.ngdc.noaa.gov/stp/space-weather/satellite-data/satellite-systems/lanl\_gps/version\_v1.10r1/ns41/. The solar wind data, geomagnetic activity indices and sunspot numbers are available from the NASA GSFC OMNI website (https://omniweb.gsfc.nasa.gov/). The results and data shown in this study can be downloaded from the UK Polar Data Centre at Meredith et al. (2025).

#### References

Agapitov, O. V., Mourenas, D., Artemyev, A. V., Mozer, F. S., Hospodarsky, G., Bonnell, J., & Krasnoselskikh, V. (2018). Synthetic empirical chorus wave model from combined Van Allen Probes and Cluster statistics. *Journal of Geophysical Research: Space Physics*, 123(1), 297–314. https://doi.org/10.1002/2017JA024843

Albert, J. M., Selesnick, R., Morley, S. K., Henderson, M. G., & Kellerman, A. (2018). Calculation of last closed drift shells for the 2013 gem radiation belt challenge events. *Journal of Geophysical Research: Space Physics*, 123(11), 9597–9611. https://doi.org/10.1029/2018JA025991
 Baker, D. N., Blake, J. B., Callis, L. B., Cummings, J. R., Hovestadt, D., Kanekal, S., et al. (1994). Relativistic electron acceleration and decay time scales in the inner and outer radiation belts: SAMPEX. *Geophysical Research Letters*, 21(6), 409–412. https://doi.org/10.1029/93GL03532

Baker, D. N., Kanekal, S. G., Horne, R. B., Meredith, N. P., & Glauert, S. A. (2007). Low-altitude measurements of 2–6 MeV electron trapping lifetimes at 1.5 < L < 2.5. Geophysical Research Letters, 34(20), L20110. https://doi.org/10.1029/2007GL031007

#### Acknowledgments

We would like to acknowledge the skill and attention to detail of Timothy J. Wehner that enabled these measurements at Medium Earth Orbit. We acknowledge Los Alamos National Laboratory for generating the BDD-IIR data products used in this study, and the National Oceanic and Atmospheric Administration's archive of the data files themselves. The research leading to these results has received funding from the Natural Environment Research Council Grants NE/V00249X/1 (Sat-Risk), NE/ X000389/1 and NE/R016038/1. M.H. and J.B. gratefully acknowledge subgrant 1559841 to the University of California, Los Angeles, from the University of Colorado Boulder under NASA Prime Grant agreement 80NSSC20K1580 and NSF GEM awards 2025706 and 2247255. Natural Environment Research Council grant NE/Z000157/1 which supports Tom A. Daggitt.

MEREDITH ET AL. 25 of 28

- Belcher, J. W., & Leverett, D. J. (1971). Large-amplitude Alfvén waves in the interplanetary medium, 2. Journal of Geophysical Research, 76, 3534. https://doi.org/10.1029/JA076i016p03534
- Blake, J. B., Baker, D. N., Turner, N., Ogilvie, K. W., & Lepping, R. P. (1997). Correlation of changes in the outer-zone relativistic-electron population with upstream solar wind and magnetic field measurements. *Geophysical Research Letters*, 24(8), 927–930. https://doi.org/10.1029/97GL00859
- Blake, J. B., Kolasinski, W. A., Fillius, R. W., & Mullen, E. G. (1992). Injection of electrons and protons with energies of tens of MeV into L < 3 on 24 March 1991. Geophysical Research Letters, 19(8), 821–824. https://doi.org/10.1029/92GL00624
- Burlaga, L. F., Klein, L., Sheeley, N. R., Jr., Michels, D. J., Howard, R. A., Koomen, M. J., et al. (1982). A magnetic cloud and a coronal mass ejection. *Geophysical Research Letters*, 9(12), 1317–1320. https://doi.org/10.1029/GL009i012p01317
- Burlaga, L. F., & Lepping, R. P. (1977). The causes of recurrent geomagnetic storms. Planetary and Space Science, 25(12), 1151–1160. https://doi.org/10.1016/0032-0633(77)90090-3
- Cabinet Office. (2012). National risk register of civil emergencies. Cabinet Office, 70 Whitehall, London. Retrieved from www.cabinetoffice.
- Cabinet Office. (2023). National risk register of civil emergencies. Cabinet Office, 70 Whitehall, London. Retrieved from www.cabinetoffice. gov.uk
- Cayton, T. E., Drake, D. M., Spencer, K. M., Herrin, M., Wehner, T. J., & Reedy, R. C. (1998). Description of the BDD-IIR: Electron and proton sensors on the GPS. Technical Report LA-UR-98-1162. Los Alamos National Laboratory.
- Cranmer, S. R. (2009). Coronal holes. Living Reviews in Solar Physics, 6, 366. https://doi.org/10.12942/lrsp-2009-3
- Daggitt, T. (2024). Electron transport, acceleration and loss in Earth's outer radiation belt. Apollo University of Cambridge Repository. https://doi.org/10.17863/CAM.112362
- Denton, M. H., & Borovsky, J. E. (2012). Magnetosphere response to high-speed solar wind streams: A comparison of weak and strong driving and the importance of extended periods of fast solar wind. *Journal of Geophysical Research*, 117(A9), A00L05. https://doi.org/10.1029/2011JA017124
- Ďurovcová, T., Šafránková, J., & Němeček, Z. (2024). How does the structure of rarefaction regions develop? *The Astrophysical Journal*, 966(1), 81. https://doi.org/10.3847/1538-4357/ad3074
- Ebert, R. W., McComas, D. J., Elliott, H. A., Forsyth, R. J., & Gosling, J. T. (2009). Bulk properties of the slow and fast solar wind and interplanetary coronal mass ejections measured by Ulysses: Three polar orbits of observations. *Journal of Geophysical Research*, 114(A1), A01109. https://doi.org/10.1029/2008JA013631
- EUSPA EO and GNSS Market Report. (2024). Retrieved from https://www.euspa.europa.eu/sites/default/files/documents/EUSPA%20Market% 20Report%202024.pdf
- Feldman, U., Landi, E., & Schwadron, N. A. (2005). On the sources of fast and slow solar wind. *Journal of Geophysical Research*, 110(A7), A07109. https://doi.org/10.1029/2004JA010918
- Fennell, J. F., Roeder, J. L., & Blake, J. B. (2012). Internal charging hazards in near-earth space: MEO and HEO orbits. Aeros. Corp., El Segundo, CA, USA, Rep. ATR-2012(8942)-4, Aug. 15.
- Frederickson, A. R., Mullen, E. G., Brautigam, D. H., Kerns, K. J., & Holman, E. G. (1991). Radiation induced insulator discharge pulses in the CRRES internal discharge monitor satellite experiment. *IEEE Transactions on Nuclear Science*, 38(6), 778–784. https://doi.org/10.1109/23.
- Gonzalez, W. D., Tsurutani, B. T., & Clua de Gonzalez, A. L. (1999). Interplanetary origin of geomagnetic storms. Space Science Reviews, 88(3–4), 529–562. https://doi.org/10.1023/A:1005160129098
- Graham, R. (1994). Killer electrons on the rise. Albuquerque Journal, B8(15 Aug).
- Grandin, M., Aikio, A. T., & Kozlovsky, A. (2019). Properties and geoeffectiveness of solar wind high-speed streams and stream interaction regions during solar cycles 23 and 24. *Journal of Geophysical Research: Space Physics*, 124(6), 3871–3892. https://doi.org/10.1029/2018JA026396
- Gubby, R., & Evans, J. (2002). Space environment effects and satellite design. *Journal of Atmospheric and Solar-Terrestrial Physics*, 64(16), 1723–1733. https://doi.org/10.1016/S1364-6826(02)00122-0
- Horne, R. B., Thorne, R. M., Shprits, Y. Y., Meredith, N. P., Glauert, S. A., Smith, A. J., et al. (2005). Wave acceleration of electrons in the Van Allen radiation belts. *Nature*, 437(7056), 227–230. https://doi.org/10.1038/nature03939
- Hua, M., & Bortnik, J. (2024). Upper limit of outer belt electron acceleration and their controlling geomagnetic conditions: A comparison of storm and non-storm events. Geophysical Research Letters, 51(13), e2024GL109612. https://doi.org/10.1029/2024GL109612
- Hua, M., Bortnik, J., Chu, X., Aryan, H., & Ma, Q. (2022). Unraveling the critical geomagnetic conditions controlling the upper limit of electron fluxes in the Earth's outer radiation belt. *Geophysical Research Letters*, 49(22), e2022GL101096. https://doi.org/10.1029/2022GL101096
- Hua, M., Bortnik, J., & Ma, Q. (2022). Upper limit of outer radiation belt electron acceleration driven by whistler-mode chorus waves. Geophysical Research Letters, 49(15), e2022GL099618. https://doi.org/10.1029/2022GL099618
- Hua, M., Bortnik, J., Spence, H. E., & Reeves, G. D. (2023). Testing the key processes that accelerate outer radiation belt relativistic electrons during geomagnetic storms. Frontiers in Astronomy and Space Sciences, 10, 1168636. https://doi.org/10.3389/fspas.2023.1168636
- Iles, R. H. A., Fazakerley, A. N., Johnstone, A. D., Meredith, N. P., & Bühler, P. (2002). The relativistic electron response in the outer radiation belt during magnetic storms. *Annales Geophysicae*, 20(7), 957–965. https://doi.org/10.5194/angeo-20-957-2002
- Jaynes, A. N., Baker, D. N., Singer, H. J., Rodriguez, J. V., Loto'aniu, T. M., Ali, A. F., et al. (2015). Source and seed populations for relativistic electrons: Their roles in radiation belt changes. *Journal of Geophysical Research: Space Physics*, 120(9), 7240–7254. https://doi.org/10.1002/201514.021234
- Koons, H. C., & Fennel, J. F. (2006). Space weather effects on communications satellites. URSI Radio Science Bulletin, 316, 27–41.
- Kozyra, J. U., Crowley, G., Emery, B. A., Fang, X., Maris, G., Mlynczak, M. G., et al. (2006). Response of the upper/middle atmosphere to coronal holes and powerful high-speed solar wind streams in 2003. In B. T. Tsurutani (Ed.), Corotating solar wind streams and recurrent geomagnetic activity, Geophysical monograph series (Vol. 167, pp. 319–340). AGU. https://doi.org/10.1029/167gm24
- Krieger, A. S., Timothy, A. F., & Roelof, E. C. (1973). A coronal hole and its identification as the source of a high velocity solar wind stream. Solar Physics, 29(2), 505–525. https://doi.org/10.1007/BF00150828
- Kwon, R.-Y., & Vourlidas, A. (2018). The density compression ratio of shock fronts associated with coronal mass ejections. *Journal of Space Weather and Space Climate*, 8, A08. https://doi.org/10.1051/swsc/2017045
- Li, W., & Hudson, M. K. (2019). Earth's Van Allen radiation belts: From discovery to the Van Allen Probes era. *Journal of Geophysical Research:* Space Physics, 124(11), 8319–8351. https://doi.org/10.1029/2018JA025940
- Li, W., Thorne, R. M., Angelopoulos, V., Bortnik, J., Cully, C. M., Ni, B., et al. (2009). Global distribution of whistler-mode chorus waves observed on the THEMIS spacecraft. *Geophysical Research Letters*, 36(9), L09104. https://doi.org/10.1029/2009GL037595

MEREDITH ET AL. 26 of 28

15427390, 2025, 11, Down

- Li, W., Thorne, R. M., Bortnik, J., Baker, D. N., Reeves, G. D., Kanekal, S. G., et al. (2015). Solar wind conditions leading to efficient radiation belt electron acceleration: A superposed epoch analysis. *Geophysical Research Letters*, 42(17), 6906–6915. https://doi.org/10.1002/ 2015GL065342
- Liu, Y., Davies, J. A., Luhmann, J. G., Vourlidas, A., Bale, S. D., & Lin, R. P. (2010). Geometric triangulation of imaging observations to track coronal mass ejections continuously out to 1 AU. *The Astrophysical Journal Letters*, 710, L82–L87. https://doi.org/10.1088/2041-8205/710/
- Ma, D., Bortnik, J., Ma, Q., Hua, M., & Chu, X. (2024). Machine learning interpretability of outer radiation belt enhancement and depletion events. Geophysical Research Letters, 51(1), e2023GL106049. https://doi.org/10.1029/2023GL106049
- Meredith, N., Bortnik, J., Hua, M., Cayton, T., Clilverd, M., Daggitt, T., & Bunting, K. (2025). Solar wind and geomagnetic conditions that lead to the largest relativistic electron fluxes in GPS orbit (version 1.0) [Dataset]. NERC EDS UK Polar Data Centre. https://doi.org/10.5285/b6d3de94-c1db-42f6-9342-061f6b74d99c
- Meredith, N. P., Cain, M., Horne, R. B., Thorne, R. M., Summers, D., & Anderson, R. R. (2003). Evidence for chorus-driven electron acceleration to relativistic energies from a survey of geomagnetically disturbed periods. *Journal of Geophysical Research*, 108(A6), 1248. https://doi.org/ 10.1029/2002JA009764
- Meredith, N. P., Cayton, T. E., Cayton, M. D., & Horne, R. B. (2023). Extreme relativistic electron fluxes in GPS orbit: Analysis of NS41 BDD-IIR data. Space Weather, 21(6), e2023SW003436. https://doi.org/10.1029/2023SW003436
- Meredith, N. P., Cayton, T. E., Cayton, M. D., & Horne, R. B. (2024). Strong relativistic electron flux events in GPS orbit. Space Weather, 22(12), e2024SW004042. https://doi.org/10.1029/2024SW004042
- Meredith, N. P., Horne, R. B., & Anderson, R. R. (2001). Substorm dependence of chorus amplitudes: Implications for the acceleration of electrons to relativistic energies. *Journal of Geophysical Research*, 106(A7), 13165–13178. https://doi.org/10.1029/2000JA900156
- Meredith, N. P., Horne, R. B., Shen, X.-C., Li, W., & Bortnik, J. (2020). Global model of whistler mode chorus in the near-equatorial region (lλml < 18°). Geophysical Research Letters, 47(11), e2020GL087311. https://doi.org/10.1029/2020GL087311
- Meredith, N. P., Horne, R. B., Sicard-Piet, A., Boscher, D., Yearby, K. H., Li, W., & Thorne, R. M. (2012). Global model of lower band and upper band chorus from multiple satellite observations. *Journal of Geophysical Research*, 117, A10225. https://doi.org/10.1029/2012JA017978
- Mishra, W., Sahani, P. S., Khuntia, S., & Chakrabarty, D. (2024). Distribution and recovery phase of geomagnetic storms during solar cycles 23
- and 24. Monthly Notices of the Royal Astronomical Society, 530(3), 3171–3182. https://doi.org/10.1093/mnras/stae1045
  Miyoshi, Y., & Kataoka, R. (2008). Flux enhancement of the outer radiation belt electrons after the arrival of stream interaction regions. Journal of
- Geophysical Research, 113(A3), A03S0. https://doi.org/10.1029/2007JA012506
  Miyoshi, Y., Kataoka, R., Kasahara, Y., Kumamoto, A., Nagai, T., & Thomsen, M. F. (2013). High-speed solar wind with southward inter-
- Miyoshi, Y., Kataoka, R., Kasahara, Y., Kumamoto, A., Nagai, T., & Thomsen, M. F. (2013). High-speed solar wind with southward interplanetary magnetic field causes relativistic electron flux enhancement of the outer radiation belt via enhanced condition of whistler waves. *Geophysical Research Letters*, 40(17), 4520–4525. https://doi.org/10.1002/grl.50916
- Nolte, J. T., Krieger, A. S., Timothy, A. F., Gold, R. E., Roelof, E. C., Vaiana, G., et al. (1976). Coronal holes as sources of solar wind. *Solar Physics*, 46(2), 303–322. https://doi.org/10.1007/BF00149859
- O'Brien, T. P., McPherron, R. L., Sornette, D., Reeves, G. D., Friedel, R., & Singer, H. J. (2001). Which magnetic storms produce relativistic electrons at geosynchronous orbit? *Journal of Geophysical Research*, 106(A8), 15533–15544. https://doi.org/10.1029/2001JA000052
- Olson, W. P., & Pfitzer, K. (1977). Magnetospheric magnetic field modelling annual scientific report. Air Force Office of Scientific Research. Pinto, V. A., Kim, H.-J., Lyons, L. R., & Bortnik, J. (2018). Interplanetary parameters leading to relativistic electron enhancement and persistent depletion events at geosynchronous orbit and potential for prediction. Journal of Geophysical Research: Space Physics, 123(2), 1134–1145. https://doi.org/10.1002/2017JA024902
- Reeves, G. D., McAdams, K. L., Friedel, R. H. W., & O'Brien, T. P. (2003). Acceleration and loss of relativistic electrons during geomagnetic storms. *Geophysical Research Letters*, 30(10), 1529. https://doi.org/10.1029/2002GL016513
- Richardson, I., & Cane, H. (2024). Near-Earth interplanetary coronal mass ejections since January 1996. Harvard Dataverse, V2. https://doi.org/10.7910/DVN/C2MHTH
- Richardson, I. G., Webb, D. F., Zhang, J., Berdichevsky, D. B., Biesecker, D. A., Kasper, J. C., et al. (2006). Major geomagnetic storms (Dst <=-100 nT) generated by corotating interaction regions. *Journal of Geophysical Research*, 111(A7), A07S09. https://doi.org/10.1029/20051A011476
- Ripoll, J.-F., Claudepierre, S. G., Ukhorskiy, A. Y., Colpitts, C., Li, X., Fennell, J., & Crabtree, C. (2020). Particle dynamics in the Earth's radiation belts: Review of current research and open questions. *Journal of Geophysical Research: Space Physics*, 125(5), e2019JA026735. https://doi.org/10.1029/2019JA026735
- Robbrecht, E., Berghmans, D., & Van der Linden, R. A. M. (2009). Automated LASCO CME catalog for solar cycle 23: Are CMEs scale invariant? Astrophysical Journal, 691(2), 1222–1234. https://doi.org/10.1088/0004-637X/691/2/1222
- Rodgers, D. J., & Ryden, K. A. (2001). Internal charging in space. In R. A. Harris (Ed.), Proceedings of 7th spacecraft charging technology conference, Noordwijk, the Netherlands, 23-27 April, ESA SP-476 (p. 25). European Space Agency.
- Roederer, J. G. (1967). On the adiabatic motion of energetic particles in a model magnetosphere. *Journal of Geophysical Research*, 72(3), 981–992. https://doi.org/10.1029/JZ072i003p00981
- Satellite Industry Association. (2025). State of the satellite industry report 2025. Retrieved from https://sia.org/news-resources/state-of-the-satellite-industry-report
- Sawadogo, S., Gnabahou, D. A., Pahima, T., & Ouattara, F. (2024). Solar activity: Towards a standard classification of solar phases from cycle 1 to cycle 24. Advances in Space Research, 73, 1041–1049. https://doi.org/10.1016/j.asr.2023.11.011
- Schwenn, R., dal Lago, A., Huttunen, E., & Gonzalez, W. D. (2005). The association of coronal mass ejections with their effects near the Earth. Annales Geophysicae, 23(3), 1033–1059. https://doi.org/10.5194/angeo-23-1033-2005
- Shen, X.-C., Hudson, M. K., Jaynes, A., Shi, Q., Tian, A., Claudepierre, S., et al. (2017). Statistical study of the storm time radiation belt evolution during Van Allen Probes era: CME- versus CIR-driven storms. *Journal of Geophysical Research: Space Physics*, 122(8), 8327–8339. https://doi.org/10.1002/2017JA024100
- Shi, R., Summers, D., Ni, B., Fennell, J. F., Blake, J. B., Spence, H. E., & Reeves, G. D. (2016). Survey of radiation belt energetic electron pitch angle distributions based on the Van Allen Probes MagEIS measurements. *Journal of Geophysical Research: Space Physics*, 21(2), 1078–1090. https://doi.org/10.1002/2015JA021724
- Shprits, Y. Y., Elkington, S. R., Meredith, N. P., & Subbotin, D. A. (2008). Review of modeling of losses and sources of relativistic electrons in the outer radiation belt I: Radial transport. *Journal of Atmospheric and Solar-Terrestrial Physics*, 70(14), 1679–1693. https://doi.org/10.1016/j.jastp.2008.06.008

MEREDITH ET AL. 27 of 28

- Shprits, Y. Y., Subbotin, D. A., Meredith, N. P., & Elkington, S. R. (2008). Review of modeling of losses and sources of relativistic electrons in the outer radiation belt II: Local acceleration and loss. *Journal of Atmospheric and Solar-Terrestrial Physics*, 70(14), 1694–1713. https://doi.org/10.1016/j.jastp.2008.06.014
- Shue, J.-H., Song, P., Russell, C. T., Steinberg, J. T., Chao, J. K., Zastenker, G., et al. (1998). Magnetopause location under extreme solar wind conditions. *Journal of Geophysical Research*, 103(A8), 17691–17700. https://doi.org/10.1029/98JA01103
- Siscoe, G. L., Goldstein, B., & Lazarus, A. J. (1969). An east-west asymmetry in the solar wind velocity. *Journal of Geophysical Research*, 74(7), 1759–1762. https://doi.org/10.1029/JA074i007p01759
- Thorne, R., Li, W., Ni, B., Ma, Q., Bortnik, J., Chen, L., et al. (2013). Rapid local acceleration of relativistic radiation-belt electrons by magnetospheric chorus. *Nature*, 504(7480), 411–414. https://doi.org/10.1038/nature12889
- Thorne, R. M. (2010). Radiation belt dynamics: The importance of wave-particle interactions. *Geophysical Research Letters*, 37(22), L22107. https://doi.org/10.1029/2010GL044990
- Tsurutani, B. T., Gonzalez, W. D., Gonzalez, A. L. C., Tang, F., Arballo, J. K., & Okada, M. (1995). Interplanetary origin of geomagnetic activity in the declining phase of the solar cycle. *Journal of Geophysical Research*, 100(A11), 21717–21733. https://doi.org/10.1029/95JA01476
- Tsyganenko, N. A., Singer, H. J., & Kasper, J. C. (2003). Storm-time distortion of the inner magnetosphere: How severe can it get? *Journal of Geophysical Research*, 108(A5), 1209. https://doi.org/10.1029/2002JA009808
- Tsyganenko, N. A., & Sitnov, M. I. (2005). Modeling the dynamics of the inner magnetosphere during strong geomagnetic storms. *Journal of Geophysical Research*, 110(A3), A03208. https://doi.org/10.1029/2004JA010798
- Tu, W., Cunningham, G. S., Chen, Y., Morley, S. K., Reeves, G. D., Blake, J. B., et al. (2014). Event-specific chorus wave and electron seed population models in DREAM3D using the Van Allen Probes. *Geophysical Research Letters*, 41(5), 1359–1366. https://doi.org/10.1002/2013GL058819
- Turner, D., Shprits, Y., Hartinger, M., & Angelopoulos, V. (2012). Explaining sudden losses of outer radiation belt electrons during geomagnetic storms. *Nature Physics*, 8(3), 208–212. https://doi.org/10.1038/nphys2185
- Turner, D. L., Kilpua, E. K. J., Hietala, H., Claudepierre, S. G., O'Brien, T. P., Fennell, J. F., et al. (2019). The response of Earth's electron radiation belts to geomagnetic storms: Statistics from the Van Allen Probes era including effects from different storm drivers. *Journal of Geophysical Research: Space Physics*, 124(2), 1013–1034. https://doi.org/10.1029/2018JA026066
- Turner, N. E., Mitchell, E. J., Knipp, D. J., & Emery, B. A. (2006). Energetics of magnetic storms driven by corotating interation regions: A study of geoeffectiveness. In B. T. Tsurutani (Ed.), Co-rotating solar wind streams and recurrent geomagnetic activity, geophysical monograph series (Vol. 167, pp. 113–340). AGU.
- Webb, D. F., Cliver, E. W., Crooker, N. U., Cyr, O. C. S., & Thompson, B. J. (2000). Relationship of halo coronal mass ejections, magnetic clouds, and magnetic storms. *Journal of Geophysical Research*, 105(A4), 7491–7508. https://doi.org/10.1029/1999JA000275
- Webb, D. F., & Howard, R. A. (1994). The solar cycle variation of coronal mass ejections and the solar wind mass flux. *Journal of Geophysical Research*, 99(A3), 4201–4220. https://doi.org/10.1029/93JA02742
- Wrenn, G. L., Rodgers, D. J., & Ryden, K. A. (2002). A solar cycle of spacecraft anomalies due to internal charging. *Annales Geophysicae*, 20(7), 953–956. https://doi.org/10.5194/angeo-20-953-2002
- Zhang, K., Li, X., Zhao, H., Xiang, Z., Khoo, L. Y., Zhang, W., et al. (2021). Upper limit of electron fluxes observed in the radiation belts. *Journal of Geophysical Research: Space Physics*, 126(1), e2020JA028511. https://doi.org/10.1029/2020JA028511

MEREDITH ET AL. 28 of 28